

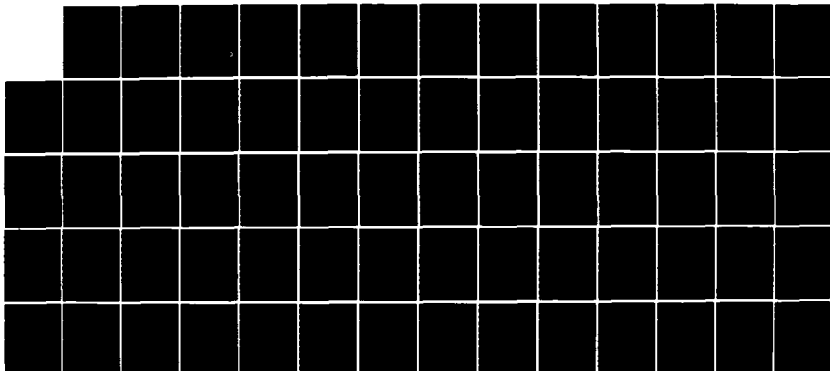
AD-A151 858

EVALUATION OF A GRIDDED IONIZATION CHAMBER FOR THE  
DETECTION OF RADIOACTI.. (U) AIR FORCE INST OF TECH  
WRIGHT-PATTERSON AFB OH SCHOOL OF ENGI.. M R GIBBONS  
MAR 84 AFIT/GNE/PH/84M-3 F/G 18/4

1/1

UNCLASSIFIED

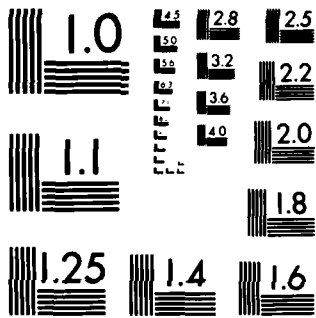
NL



END

FILED

DTIC



MICROCOPY RESOLUTION TEST CHART  
NATIONAL BUREAU OF STANDARDS-1963-A

1

AD-A151 850



EVALUATION OF A GRIDDED IONIZATION  
 CHAMBER FOR THE DETECTION OF  
 RADIOACTIVE NOBLE GASES

THESIS

Matthew R. Gibbons  
 Second Lieutenant, USAF

AFIT/GNE/PH/84M-3

DTIC FILE COPY

**DISTRIBUTION STATEMENT A**  
 Approved for public release  
 Distribution Unlimited

DTIC  
 ELECTE  
 MAR 29 1985  
 S B D

DEPARTMENT OF THE AIR FORCE  
 AIR UNIVERSITY (ATC)  
**AIR FORCE INSTITUTE OF TECHNOLOGY**

Wright-Patterson Air Force Base, Ohio

85 03 13 106

REPRODUCED AT GOVERNMENT EXPENSE

AFIT/GNE/PH/84M-3

EVALUATION OF A GRIDDED IONIZATION  
CHAMBER FOR THE DETECTION OF  
RADIOACTIVE NOBLE GASES

THESIS

Matthew R. Gibbons  
Second Lieutenant, USAF

AFIT/GNE/PH/84M-3

DTIC  
ELECTE  
MAR 29 1985  
S D  
B

Approved for public release; distribution unlimited

AFIT/GNE/PH/84M-3

EVALUATION OF A GRIDDED IONIZATION CHAMBER FOR THE  
DETECTION OF RADIOACTIVE NOBLE GASES

THESIS

Presented to the Faculty of the School of Engineering  
of the Air Force Institute of Technology  
Air University

In Partial Fulfillment of the  
Requirements for the Degree of  
Master of Science in Nuclear Engineering

Matthew R. Gibbons, B.S.  
Second Lieutenant, USAF

March 1984

Approved for public release; distribution unlimited



## Table of Contents

	Page
Preface . . . . .	ii
List of Figures . . . . .	v
List of Tables . . . . .	vi
Abstract . . . . .	vii
I. Introduction . . . . .	1
Background . . . . .	1
Problem and Scope . . . . .	2
Approach . . . . .	2
Sequence of Presentation . . . . .	3
II. Theory . . . . .	5
Ionizing Radiation . . . . .	5
Pulse Formation . . . . .	7
Efficiency . . . . .	11
Energy Resolution . . . . .	17
III. The Detecting Gases and the Sources . . . . .	19
Xenon and Argon . . . . .	19
Xenon-131m and Xenon-133 . . . . .	19
Bismuth-207 . . . . .	23
Uranium-233 . . . . .	24
The Gamma Ray Sources . . . . .	25
IV. Equipment . . . . .	26
The Detector . . . . .	26
The Gas Handling System . . . . .	29
V. Procedure . . . . .	32
Gas Purification . . . . .	32
Sample Introduction . . . . .	33
Data Collection . . . . .	34

	Page
VI. Results . . . . .	35
Initial Considerations . . . . .	35
The Exterior Sources . . . . .	36
Interior Sources . . . . .	43
VII. Conclusions and Recommendations . . . . .	51
Conclusions . . . . .	51
Recommendations . . . . .	52
Bibliography . . . . .	55
Appendix: Discharge in Gases . . . . .	57
Vita . . . . .	60

List of Figures

Figure	Page
1. The Simplified Ionization Chamber . . . . .	8
2. Electron Mobilities in Liquified Noble Gases . . . . .	10
3. Xenon-131m Decay Scheme . . . . .	21
4. Xenon-133 Decay Scheme . . . . .	21
5. The Combined Spectrum of Xenon-131m and Xenon-133 . . . . .	21
6. The Bismuth-207 Decay Scheme . . . . .	23
7. Bismuth-207 Energy Spectra . . . . .	24
8. The Ionization Chamber . . . . .	27
9. The Supporting Electronics for the Ionization Chamber . . . . .	29
10. The Gas Handling System . . . . .	30
11. Americium-241 Electron Drift Velocity Study . . . . .	37
12. The $\gamma$ ray Sources Energy Spectra . . . . .	40
13. Pulse Height vs Electric Field ( $\text{Co}^{57}$ ) . . . . .	41
14. Pulse Height vs Electric Field ( $\text{Bi}^{207}$ ) . . . . .	44
15. Fraction of Electrons Passed vs $E_a/E_c$ . . . . .	46
16. Decrease in Grid Voltage with -5.0 kV on the Cathode . . . . .	47
17. The Uranium-233 4.82 Mev Alpha Peak . . . . .	49
18. The Xenon-131m and Xenon-133 Combined Spectrum . . . . .	50
19. A Liquid Noble Gas Proportional Counter . . . . .	53
20. The Ionization Coefficient in Various Gases . . . . .	58
21. The Secondary Emission Coefficient . . . . .	58
22. Paschen Curves . . . . .	58

List of Tables

Table	Page
I. The $\alpha$ Constants for Oxygen Impurities . . . . .	16
II. Energy Resolution of a 1 MeV Particle in LA and LXe . . . . .	17
III. Some Physical Properties of Xenon and Argon . . . . .	20
IV. Nuclear Decay Schemes of Xenon-131m and Xenon-133 . . . . .	22
V. Uranium-233 and its Progeny . . . . .	24
VI. The Efficiency Fractions . . . . .	38
VII. The $\gamma$ ray Source Counting Rates . . . . .	39

Abstract

This study investigates the feasibility of quantifying the constituents of a radioactive noble gas sample with a liquid noble gas gridded ionization chamber.  $Xe^{131m}$  and  $Xe^{133}$  are the noble gases used to test the chamber. Several other sources are used to characterize other aspects of the chamber. The chamber is designed to hold the liquid noble gas between the cathode and the grid while vapor remains between the anode and the grid. Thus the ionization caused by the radioactive noble gas sample is confined for the most part between the grid and the cathode. In this way position dependence of generated voltage pulse heights is eliminated. The efficiencies found for the detector are high, but the energy resolution is only 40% fwhm. The poor resolution is due to limited electric fields in the chamber, 2.4 kV/cm. Discharge in the vapor prevented higher electric fields in the chamber. Without good energy resolution, ratios of radioactive noble gases in a sample can not be found. Some possible solutions to the energy resolution problem are presented.

EVALUATION OF A GRIDDED IONIZATION  
CHAMBER FOR THE DETECTION OF  
RADIOACTIVE NOBLE GASES

I Introduction

Background

Nuclear reactors, nuclear weapons, natural processes and other phenomena can cause the release of radioactive noble gases into the atmosphere. These gases can be separated from samples of air and analyzed. The study of the quantities of these gases and the ratios of their isotopes can help in the determination of their origin.

Previous studies have used scintillation counters and germanium semi-conductor detectors. The scintillation counters prove to have high efficiency since the gas can be dissolved into the scintillation liquid. The problem with scintillation counters is their relatively poor resolution. The resolution of the germanium detectors is much better, but only small gas samples may be used with these detectors. Also low energy photons are absorbed by the containers for the gas.

In an effort to obtain high efficiency and good resolution several previous AFIT students have analyzed radionuclides of xenon with Si(Li) detectors (1). Identification of the radionuclides under study was possible, but a highly accurate quantitative analysis of the radionuclides could not be made. The detection system suffered from low efficiency and self-absorption of internal conversion electrons.

In order to overcome these problems a liquid noble gas ionization chamber was constructed. This is a high efficiency detector since the

radioactive noble gas sample can be mixed in with the detecting medium. The detector should also have good resolution. The energy resolution found by several researchers for the 976 keV internal conversion electron peak of Bi<sup>207</sup> is 34 keV fwhm (25:255). The energy resolution is much better than the energy resolution of scintillation counters.

Two other AFIT students, Berggren and Benedetti, designed and studied liquid noble gas ionization chambers. Berggren found that pulse heights were dependent on the position of energy deposition in the chamber (2). Also corona discharge tended to limit the maximum obtainable detector bias. Benedetti constructed a parallel plate chamber with a Frisch grid in order to remove the position dependence of the pulse heights.

#### Problem and Scope

The objective of this thesis is to continue the study of the liquid noble gas ionization chamber. The operating characteristics and the energy resolution of the system are the major areas of concern. The detector must have good resolution with a radioactive noble gas as an internal source.

Xenon and argon are used as the detection media inside the chamber. Samples of Xe<sup>131m</sup> and Xe<sup>133</sup> serve as the noble gas radioisotopes. Quantitative and qualitative differentiation of these isotopes is the criterion for the successful operation of this detection system.

#### Approach

The research began with the construction of a new ionization chamber. The chamber was made to increase the uniformity of the electric field in the detection medium. The probability of corona discharge in

the chamber was also reduced.

The chamber was then tested with a number of different sources before the radioactive xenon was introduced. This was done to determine whether the chamber was functioning properly since the radioactive xenon sample was limited.

Gamma ray sources were placed external to the chamber. In this way the operating characteristics could be roughly determined. Also the sources could be removed so that the magnitude of the background could be found.

Solid sources of Bi<sup>207</sup> and U<sup>233</sup> were then placed inside the chamber on the cathode. These gave data on the chamber response to internal conversion electrons, beta particles and alpha particles. Since these sources rested on the cathode, any complexities due to a source spread throughout the detecting volume were eliminated.

Finally, the radioactive xenon samples were studied. During the runs, liquid argon was used first as the detecting medium because of its lower cost.

#### Sequence of Presentation

The theory of operation of a gridded ionization chamber is presented in Chapter II. Recombination and electron attachment effects in such a chamber are also discussed. Theoretical calculations for the chamber efficiency are included as well.

Decay schemes of the radioactive sources are tabulated in Chapter III. The schemes are abbreviated to include only those radiations which are of interest to the study. This chapter also includes the physical characteristics of the ionization chamber media.

Chapter IV contains the detection system design, and Chapter V lists the procedure for operation of the system. The results obtained are presented and discussed in Chapter VI. The conclusions and recommendations of the study are in Chapter VII.

## II Theory

An ionization chamber operates through the collection of electrons and positive ions produced by the passage of radiation into the chamber. Thus the effects caused by the radiation in the detecting material of the chamber must be known. The determination of the number of charges produced and the efficiency of collection of these charges must also be understood. An estimate of the energy resolution of the detector is presented for comparison with the actual resolution obtained.

### Ionizing Radiation

Beta and Alpha Particles. Two types of charged particles emitted by radioactive sources are beta and alpha particles. These charged particles interact mainly through coulombic attraction and repulsion with the electrons and nuclei of the neutral atoms in matter. The interactions cause electrons to be stripped from the atoms.

The beta and alpha particles eventually come to rest after depositing their kinetic energy in this manner. The result is a track of ion pairs. The number of ion pairs formed depends on the initial energy of the particle, and the average energy loss per ion pair formed. The average energy lost is called the W value. The W values for liquid argon and xenon are 23.6 eV and 15.8 eV respectively (25:257).

Photons. Gamma ray photons emitted by certain radionuclides also interact with the detector medium. The gammas of interest in this study are of lower energies (less than 0.2 MeV). Their main interaction mechanisms are photoelectric absorption and Compton scattering.

In the photoelectric effect the photon transfers all of its energy

to an atom as a whole. This energy is then transferred to an electron. Since the binding energy of the electron is usually negligible, most of the energy transferred to the electron manifests itself as kinetic energy. The electron then acts in the same manner as a beta particle leaving a track of ion pairs. The number of ion pairs is basically directly proportional to the initial photon energy.

In Compton scattering the photon interacts with an orbiting electron. The electron is considered a free electron as long as the photon energy is large compared to the electron binding energy. The interaction results in a scattered photon and a recoil electron. The energy transferred to the electron is less than that of the initial photon. The electron again creates a track of ion pairs.

Ranges. The distance which a charged particle travels through a material is its range. The range can be calculated from tables provided by various sources (24:155). Since the purpose of the chamber is to study the various electrons emitted by  $Xe^{131m}$  and  $Xe^{133}$ , the range of the most energetic of these electrons determines the size of the chamber. The section on efficiency discusses this.

Absorption of Photons. Since the chamber is initially calibrated with gamma emitting sources, the number of photons stopped in the chamber must be known. This is given by the equation

$$N = N_0 \exp(-(\mu/\rho)\rho x) \quad (1)$$

where

$N_0$  is the initial number of photons entering the detector

$\mu/\rho$  is the mass attenuation coefficient in  $cm^2/g$

$\rho$  is the density of the detector medium

x is the distance traveled through the detector medium

The mass attenuation coefficients for the elements are tabulated (21). The coefficients depend on the type of interaction and the energy of the photon.

#### Pulse Formation

The Parallel Plate Chamber. One method of collecting the ion pairs produced in the chamber is to use parallel conducting plates. With one plate set at a negative potential and the other set at zero potential an electric field is set up which causes the electrons and positive ions to move toward the plates of opposite charge. The movement of the charges causes a change in the potential of the anode. This change in potential is measured as a voltage pulse.

The change in potential on the collecting electrode has been derived by Knoll and others (17:176). It takes the form

$$P(t) = \text{Net } (w_+ + w_-)/Cd \quad (2)$$

where

N is the number of ion pairs

e is the electronic charge

t is the time

C is the capacitance of the system

d is the separation of the electrodes

$w_+, w_-$  are the velocities of the positive ions and electrons

The potential induced on the collector by the ion pairs from one track must be removed after the ions reach the plates so that the potential induced by subsequent ion tracks can be measured. The result is a voltage pulse indirectly caused by each particle of ionizing radiation. Usually a preamplifier performs this task, but for illustra-

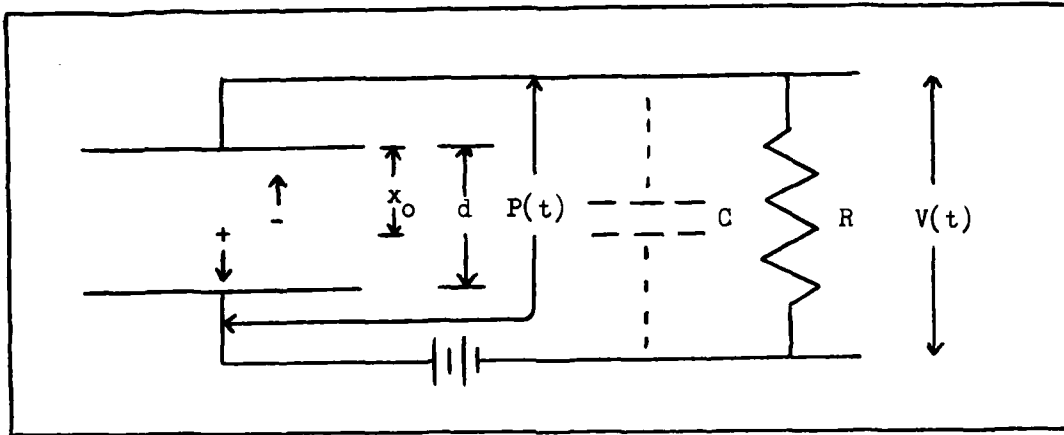


Fig. 1. The Simplified Ionization Chamber

tive purposes a simple RC circuit is considered here.

Since the drift velocity of the massive positive ions is much less than that of the electrons, the time constant of the RC circuit is set at much less than the positive ion collecting time. Only the electrons are collected by the time the voltage pulse decays. The chamber is ready to receive another pulse much sooner.

During the time that the electrons are collected, the positive ion motion can be neglected. The time dependent potential simplifies to

$$P(t) = -New_t/Cd \quad (3)$$

The following differential equation describes the potential,  $V(t)$ , which one finds on the output side of the RC circuit (26:93).

$$dP/dt = dV/dt + V/RC \quad (4)$$

For RC much less than one this becomes

$$dP/dt = V/RC \quad (5)$$

Thus the measured potential is

$$V(t) = -New_{RC} (1 - \exp(-t/RC))/Cd \quad (6)$$

After the electrons are collected the potential measured is

$$V(t) = -New_R (\exp(x_o/RCw_) - 1) \exp(-t/RC)/d \quad (7)$$

With all variables held constant except for N, the maximum amplitude of the voltage pulse is proportional to the energy of the initial ionizing particle. But this equation shows two important variables which affect the maximum amplitude of the voltage pulse. The first is the electron drift velocity. A larger drift velocity for a given plate separation causes a larger voltage pulse.

The second variable is the initial ion pair location,  $x_o$ . The amplitudes of the voltage pulses are proportional to the energy of the initial radiation only if all of the ion pair tracks are formed in the same location in the chamber. This is not a practical situation. Problems of this sort were reported by Berggren in previous work with the liquid noble gas ionization chamber (2). The solution to this problem is the Frisch grid.

Electron Drift Velocity. The main concern with the drift of the electrons is to allow them to be collected before the decay of the voltage pulse. By using larger and larger shaping times on the voltage pulse a maximum amplitude can be reached. This represents the time needed to collect the electrons. With the known separation of the plates the electron drift velocity is calculable. Others have calculated the drift velocity of electrons in liquid noble gases. Some of their results are shown in Figure 2.

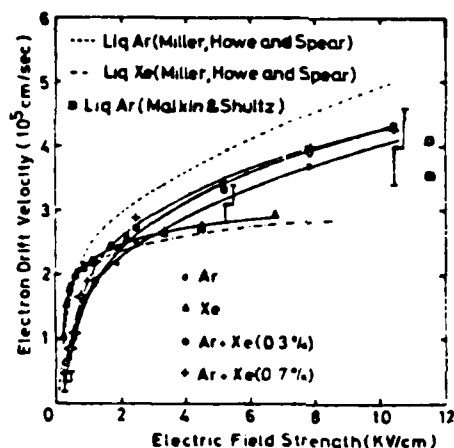


Fig. 2. Electron Mobilities in Liquified Noble Gases (25:4)

The Frisch Grid. A grid consisting of evenly spaced parallel wires can eliminate the dependence of the voltage pulse amplitude on the position of the initial ion pair track. A grid, inserted between the anode and the cathode, was first suggested by O. R. Frisch (5:192). If ion pairs are created only between the cathode and the grid, the grid shields the collecting anode from the charges. The anode potential changes only after the electrons move past the grid. The pulse heights are based on the constant anode to grid distance.

In an article by Bunemann the dimensions of such gridded ionization chambers are discussed (5). The dimensions are governed by the efficiency of the shielding for the anode and the extent to which electrons are allowed to pass the grid.

The shielding is measured by the amount of change in the electric field between the anode and the grid,  $E_a$ , given a change in the electric field between the cathode and the grid,  $E_c$ . The ratio of these changes is defined as the inefficiency,  $\sigma$ . The inefficiency is given by

$$\sigma = d \ln(d/2\pi r)/2\pi D_a \quad (8)$$

where

$d$  is the distance between the center of the grid wires

$r$  is the radius of the grid wires

$D_a$  is the distance from the anode to the grid

In order to assure that the electrons are collected on the anode and not on the grid, the cathode and the grid must be set at certain voltages. Assuming that the anode is at ground, the following relationship applies

$$D_c \geq D_a (1 + 2\pi r/d)(V_c - V_g)/(1 - 2\pi r/d) V_g \quad (9)$$

where

$D_c$  is the distance from the cathode to the grid

$V_c$  is the potential on the cathode

$V_g$  is the potential on the grid

The Chamber. Since the radioactive xenon is diffused throughout the detection medium, the ionization chamber must be specifically designed to take advantage of the Frisch grid. This is accomplished by liquifying the detecting noble gas only between the cathode and the grid. Vapor remains between the grid and the anode. The ionization caused in the vapor is negligible, and thus for all practical purposes ion pairs are only created between the cathode and the grid.

#### Efficiency

The efficiency of a detector is calculated as the ratio of the number of counts measured by the detector for radiation of a certain energy over the actual number of particles emitted by the source of that energy.

The number of particles emitted is given by

$$N_i = f_i S t_c \quad (10)$$

where

$f_i$  is the branching ratio for the  $i$ th particle emitted

$S$  is the activity of the source

$t_c$  is the time of the count

The efficiency of the detector depends on a number of factors. In this system the important factors include the geometry of the system, the scattering of particles outside of the chamber, and the escape of particles from the chamber. With these factors the number of counts measured can be estimated with the equation

$$C = f_g f_{ab} f_s N_i \quad (11)$$

where

$f_g$  is a geometry factor

$f_{ab}$  is the fraction of particles interacting outside of the chamber

$f_s$  is the fraction of particles stopped in the chamber

Geometry. The position of the source in relation to the chamber affects the number of ionizing particles emitted by the source which reach the chamber. Since the chamber is designed to hold the source internally, the geometry factor is one.

Geometry must still be considered for the gamma sources which were placed external to the chamber. The solid angle taken up by the surface area of the detector determines the fraction of particles which are emitted toward the detector. This fraction takes the form

$$f_g = \Omega/4\pi \quad (12)$$

For a circular detector surface of radius  $r$  and a distance from source

to detector of  $h$ , the fraction becomes

$$f_g = (1 - h/(h^2 + r^2)^{1/2})/2 \quad (13)$$

Scattering and Absorption. Particles emitted by the source may also be scattered or absorbed by materials between the source and the detector. This again only applies to sources outside of the detector. This fraction takes the form

$$f_{ab} = \exp(-(\mu/\rho)_t x) \quad (14)$$

where

$(\mu/\rho)_t$  is the total absorption coefficient for the material

$\rho$  is the density of the intervening material

$x$  is the thickness of the intervening material

This equation assumes that scattered photons will not enter the detector.

Escape. For those particles which enter or are created in the detector, the number which are stopped in the chamber must be determined. Photons again depend on the scattering and absorption cross sections. The fraction stopped is given by the equation

$$f_s = 1 - \exp(-(\mu/\rho) x) \quad (15)$$

where

$(\mu/\rho)$  is the cross section for the interaction of interest

Charged particles have a certain range in the chamber. The fraction of these particles which escape is determined by their range and their distance from the edge of the chamber.

Sources spread throughout the volume of the chamber present a unique

situation. Those charged particles created in the volume bounded by the chamber and a surface inside the chamber by a distance equal to the particle range are considered as capable of escape. In a cylindrical chamber this volume is

$$\Delta V = \pi r^2 d - \pi(r - R)^2(d - 2R) \quad (16)$$

where

$r$  is the chamber radius

$d$  is the chamber length

$R$  is the particle range

A measure of the particles escaping is this volume divided by the total chamber volume,  $V_c$ . This fraction may be further divided by four since not all of the particles are emitted in the outward direction. The fraction of particles stopped in the chamber thus becomes

$$f_s = 1 - \Delta V/4V_c \quad (17)$$

### Recombination

Recombination can prevent the collection of the electrons and ion pairs created by ionizing radiation. In a liquid noble gas chamber the main types of recombination are electron attachment and initial recombination.

Electron attachment occurs because of electronegative impurities in the detection medium. Once an electron attaches to a slow moving impurity atom it can easily recombine with a positive ion. The attachment is governed by the equation (15:153)

$$Q = 2Q_0 \lambda (1 - (\lambda/D)(1 - \exp(-D/\lambda)))/D \quad (18)$$

where

$Q$  is the detected charge

$Q_0$  is the maximum available charge

$D$  is the ionization chamber plate separation

$\lambda$  is the mean free path length for electron attachment

The mean free path length for electron attachment is determined by

$$\lambda = \alpha \bar{E}/p \quad (19)$$

where

$\bar{E}$  is the electric field

$p$  is the impurity concentration

$\alpha$  is a proportionality constant

The values of  $\alpha$  for oxygen impurities are given in Table I. The effect of nitrogen impurities is 200 times less than the effect of oxygen impurities.

Equation 19 does not fully quantify the situation for alpha particles. The high ion pair density in the initial track left by alpha particles requires the consideration of columnar recombination as discussed by Kramers (15:153). Here electrons can recombine with positive ions in the initial track before they drift away from the track. The expression for alpha particles becomes

$$Q = 2f\lambda Q_0 (1 - \exp(-D/\lambda))/D \int_0^\infty \frac{x}{f \exp(x) + 1} dx \quad (20)$$

where

$$f = \bar{E}/\bar{E}_0 \quad (21)$$

This does not consider the angle between the track and electric field lines. The term  $\bar{E}_0$  is the saturation field strength for the ion pair

TABLE I

The  $\alpha$  Constants for Oxygen Impurities

Ionizing Particle	$\alpha$ ppm cm <sup>2</sup> /kV	
	LA	LXe
alpha	.14 $\pm$ .03	---
beta	.15 $\pm$ .03	0.2

(15:154, 3:39)

column. It is given by

$$\bar{E}_0 = 4\pi^{\frac{1}{2}}eN/b \quad (22)$$

where

e is the electron charge

N is the charge density of the column

b is the diameter of the ionization column

The saturation field strength has been calculated to have a value near 800 kV/cm (15:154).

Obviously, initial recombination affects the ion pairs in beta particle tracks, but its effect is of much less importance. Electron attachment is the major concern in the energy resolution of the chamber. Ion pairs formed in different parts of the chamber travel through different amounts of liquid before reaching the grid. Since electron attachment occurs throughout the volume of the chamber, it can cause a position dependence for the magnitude of the voltage pulses. Such a dependence would decrease the energy resolution of the chamber. Hoffman found a saturation field of about 15 kV/cm for a chamber with an electrode separation of 2 mm (15:151). Oxygen impurities were less than 1 ppm, and nitrogen impurities were less than 4 ppm.

TABLE II

Energy Resolution of 1 MeV  
Particle in LA and LXe

Liquid	F	$E_n$ (keV)	$E_i$ (keV)	$E_t$ (keV)
A	0.116	3.57	3.88	5.27
Xe	0.059	2.36	2.25	3.26

(8:356-357)

Energy Resolution

The ultimate energy resolution in the ionization chamber is expressed by the full width at half maximum (fwhm) of a peak in the energy spectrum. It is calculated from the formula

$$E_t = (E_n^2 + E_i^2)^{1/2} \quad (23)$$

where

$E_n$  is the contribution from electronic noise

$E_i$  is caused by fluctuations in the initial number of ion pairs

The contribution from the fluctuation in the number of ion pairs when a particle with energy  $E_0$  deposits all of its energy is

$$E_i = 2.36 (E_0 FW)^{1/2} \quad (24)$$

where

$E_0$  is the energy of the initial particle

F is the Fano factor

W is the average energy required to form an ion pair

The Fano factors and the energy resolutions for a 1 MeV particle are given in Table II. The Fano factor is an experimentally determined value which quantifies the departure of the observed statistical fluctuations

in the number of ion pairs from pure Poisson statistics (17:92). The electronic noise factors were estimated for systems using low temperature FETs.

The values indicate an energy resolution near that of semiconductor detectors. In practice such resolutions have not been achieved. The resolution for a 1 MeV particle has been near 34 keV fwhm. As reported by Edmiston, the resolution of the detectors appears to be limited by the electronics and the geometry (9:353). Still the achieved resolutions are much better than those of liquid scintillators.

### III The Detecting Gases and the Sources

The physical characteristics of the detecting gases determine the operating conditions of the chamber. The various sources meanwhile test different aspects of the chamber. In this chapter some of the properties of argon and xenon are presented along with decay data on the sources studied.

#### Xenon and Argon

Both xenon and argon are noble gases. They are essentially chemically inert. They are ideal as ionization chamber media since they do not undergo electron attachment.

Argon makes up almost 1% of the earth's atmosphere while xenon is the rarest of the stable elements (13). Xenon has an estimated abundance of  $2.9 \times 10^{-9}\%$  of the earth's crust. Both of these elements can be obtained in commercially purified samples. The gas used in the laboratory is 99.999% pure. Table III lists some of the properties of xenon and argon.

The greater atomic mass and density of xenon allow it to stop ionizing particles and photons more easily than argon. Thus the volume of a chamber utilizing xenon may be less than that of a chamber utilizing argon. Yet the greater density of xenon may also cause an increase of recombination. Thus both elements have favorable and unfavorable characteristics.

#### Xenon-131m and Xenon-133

Both  $\text{Xe}^{133}$  and  $\text{Xe}^{131m}$  are produced in fission reactions along with a number of other noble gas radioisotopes. After three days these two isotopes and  $\text{Kr}^{85}$  are the only major radioisotopes remaining (6:76). The

TABLE III

## Some Physical Properties of Xenon and Argon

Properties	Xenon	Argon
-----		
Triple Point		
Temperature (K)	161.391	83.806
Pressure (Torr)	612.2	517.1
Density		
Solid (g/cc)	3.54	1.622
Liquid (g/cc)	3.076	1.414
Gas (mg/cc)	8.18	4.05
Liquid		
Boiling Point (K)	165.03	87.27
Density at BP (g/cc)	2.987	1.3998
Atomic Mass	131.30	39.948
-----		
(12:111)		

other noble gas isotopes have decayed or had extremely small abundances initially. Therefore, the study of these two xenon isotopes is reasonable if one wishes to obtain additional data on a fission reaction from air samples.

$\text{Xe}^{131\text{m}}$  exists in an excited state 163.93 keV above the ground state. It has a half-life of 11.8 days and decays mainly through an internal conversion electron.

$\text{Xe}^{133}$  decays by beta emission to  $\text{Cs}^{133}$ . Its half-life is 5.27 days. Almost all of these decays leave the cesium in an excited state 81 keV above the ground state. The excited state decays in  $6.3 \times 10^{-9}$  s.

Detailed nuclear decay scheme data for  $\text{Xe}^{131\text{m}}$  and  $\text{Xe}^{133}$  are listed in Table IV. The combined spectrum of the two radioisotopes should ideally resemble Figure 5. The counts in the beta spectrum and under the 164 keV peak can be compared to obtain the ratio between the two isotopes.

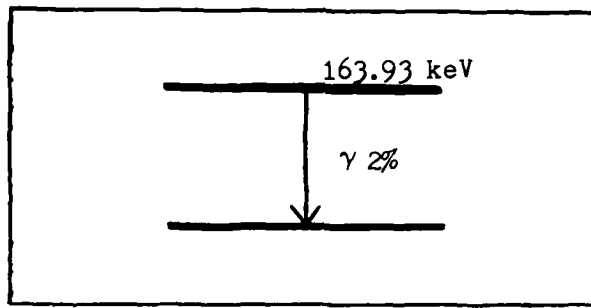


Fig. 3. Xenon-131m Decay Scheme (19:277)

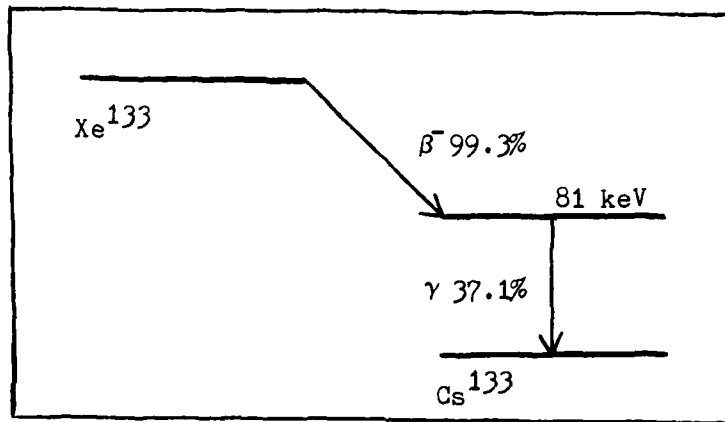


Fig. 4. Xenon-133 Decay Scheme (19:280-281)

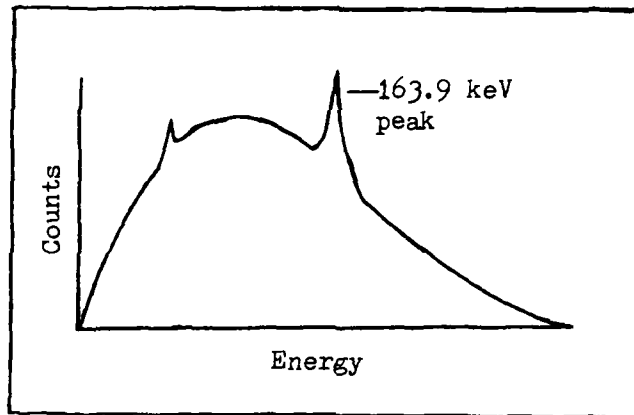


Fig. 5. The Combined Spectrum of Xenon-131m and Xenon-133

TABLE IV

## Nuclear Decay Schemes of Xenon-131m and Xenon-133

Radiation Type	Energy (keV)	Intensity (%)
$Xe^{131m}$		
Auger-L	3.43	75.0
Auger-K	24.6	6.8
ce K	129.369	61.2
ce L	158.477	28.6
ce M	162.788	6.50
ce NOP	163.722	1.78
Xray L	4.1	8.0
Xray K $_{\alpha 1}$	29.458	15.5
Xray K $_{\alpha 2}$	29.779	28.7
Xray K $_{\beta}$	33.6	10.2
$\gamma$ ray	163.93	1.96
$Xe^{133}$		
Auger-L	3.55	49.0
Auger-K	25.5	5.5
ce K	43.636	0.30
ce K $_{\alpha 1}$	45.0124	52.0
ce L $_{\alpha 2}$	75.2827	8.49
ce MNO	79.7799	2.3
$\beta^-$ maximum	346.0	
average	100.5	99.34
Xray L	4.29	6.1
Xray K $_{\alpha 1}$	30.6251	13.3
Xray K $_{\alpha 2}$	30.9728	24.6
Xray K $_{\beta}$	35	8.84
$\gamma$ ray	81	37.1

(4:321-323)

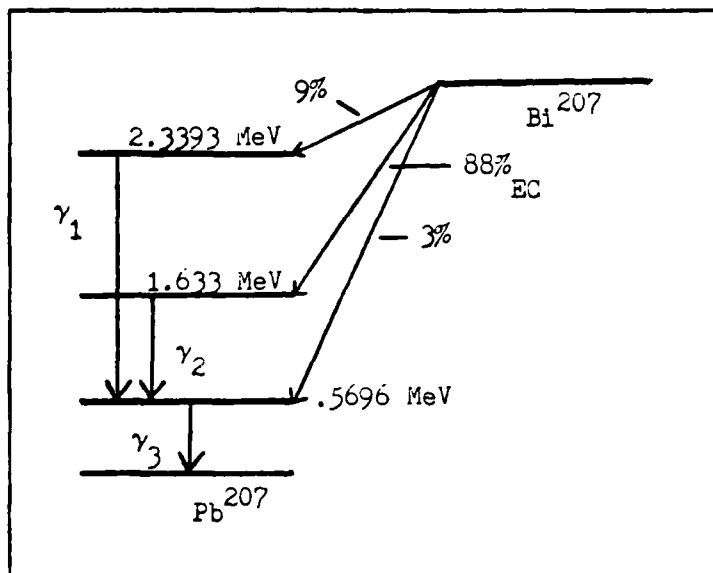


Fig. 6. The Bismuth-207 Decay Scheme (19:397)

### Bismuth-207

Bi<sup>207</sup> decays exclusively by electron capture to Pb<sup>207</sup>. The energies of the internal conversion electrons emitted by the excited states of Pb<sup>207</sup> are 0.482 MeV, 0.55 MeV, 0.975 MeV and 1.048 MeV.

The energies of gamma rays one, two and three are 1.7697 MeV, 1.0634 MeV and 0.5696 MeV. Their internal conversion to gamma ray ratios are 0.0025, 0.096 and 0.017. The 1.048 MeV and 0.55 MeV electrons are the L-conversion electrons from the 1.064 MeV and 0.5696 MeV transitions. The 0.975 MeV and 0.482 MeV electrons are the K-conversion electrons from those transitions. Energy spectra of Bi<sup>207</sup> obtained with liquid argon gridded ion chambers are shown in Figure 7. Bi<sup>207</sup> allows the detection characteristics of the chamber to be tested with high energy electrons before the introduction of radioactive xenon.

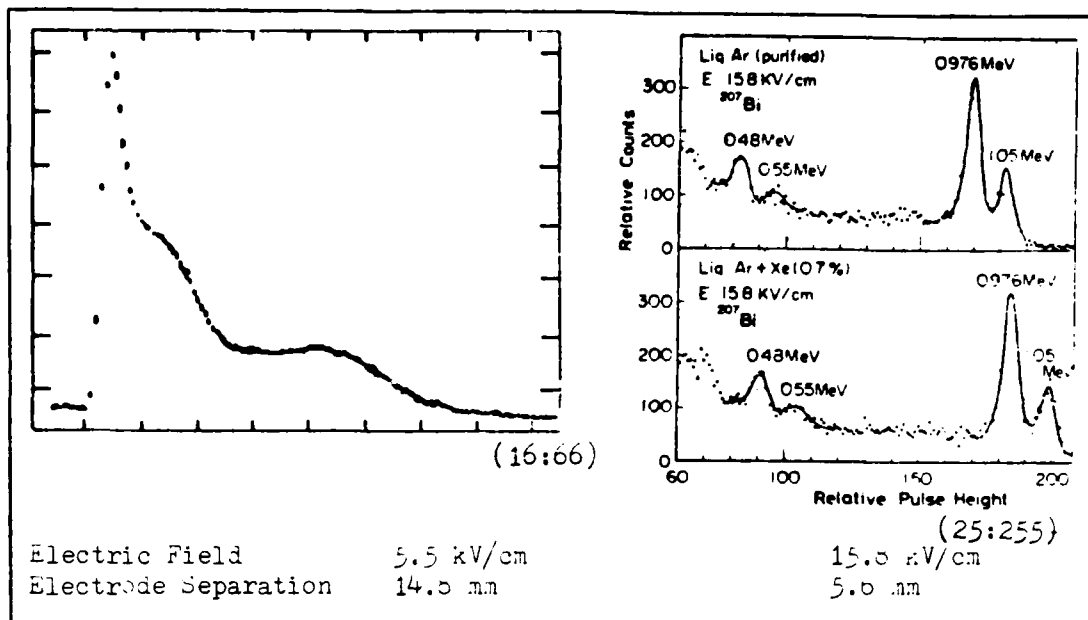


Fig. 7. Bismuth-207 Energy Spectra

### Uranium-233

$U^{233}$  is an alpha particle emitter. A few of its progeny and their emissions are listed in Table V. Because of the long half-life of Thorium, the progeny of  $U^{233}$  will not yet be in secular equilibrium. This source allows data collection on the chamber response to the 4.82 MeV alphas of  $U^{233}$ .

TABLE V

#### Uranium-233 and its Progeny

Isotope	Radiation	Energy (MeV)	Half-life
$U^{233}$	$\alpha$	4.82	$1.59 \times 10^5$ yr
$Th^{229}$	$\alpha$	4.84	7340 yr
$Ra^{225}$	$\beta^-$	0.35	14.8 d
$Ac^{225}$	$\alpha$	5.824	10.0 d
$Fr^{221}$	$\alpha$	6.34	4.8 m

(19)

### The Gamma Ray Sources

The gamma ray sources are  $\text{Am}^{241}$ ,  $\text{Cd}^{109}$ , and  $\text{Co}^{57}$ .  $\text{Am}^{241}$  is used as a gamma ray source exterior to the chamber. It decays by alpha emission to  $\text{Np}^{237}$ . Most of the decays (86%) leave the  $\text{Np}^{237}$  in an excited state 59.54 keV above the ground state. The  $\text{Cd}^{109}$  source emits an 88.03 keV gamma with a branching ratio of 0.361. Finally, the  $\text{Co}^{57}$  source emits two gamma rays of interest. They are 122 keV with a branching ratio of 0.8559 and 136 keV with a branching ratio of 0.1061. The other photons emitted by these sources are either too energetic to be stopped by the chamber or too weak to penetrate to the chamber.

#### IV Equipment

The detection system consists of two main parts. The first is the ionization chamber and its supporting electronics. The second is the gas handling system which supplies the purified noble gas to the chamber. This chapter describes these subsystems.

##### The Detector

The Chamber. The chamber itself is constructed from a Varian glass adaptor. A 1.5 in. kovar tube is attached to a 2.75 in. ConFlat flange. A 7052 glass tube is sealed to the kovar. The tube is reduced in size to form a short cylinder about 1.6 cm in diameter and 1.2 cm in length. The bottom of the cylinder is sealed to a kovar disk. The disk provides a cathode for the chamber.

Above the cylinder a kovar rod extends through the side of the chamber. The wire grid rests on a nickel tab connected to the rod. The rod itself is connected to a high voltage lead exterior to the chamber. The chamber is shown in Figure 8.

The chamber flange is bolted to a 6 in. blank ConFlat flange. This flange is supported by two 0.75 in. stainless steel tubes which also act as an inlet and outlet for liquid nitrogen. The blank flange has high voltage feedthroughs for the cathode and grid. It has insulated feedthroughs for thermocouple wires. The thermocouple wires are pressed against the kovar tube by 5 mil kovar wire which is wrapped around the tube. The flange also has a tube extending into the chamber. This tube provides an inlet for the detecting gas.

A 2.75 in. miniflange bolted to the top of the blank flange has an

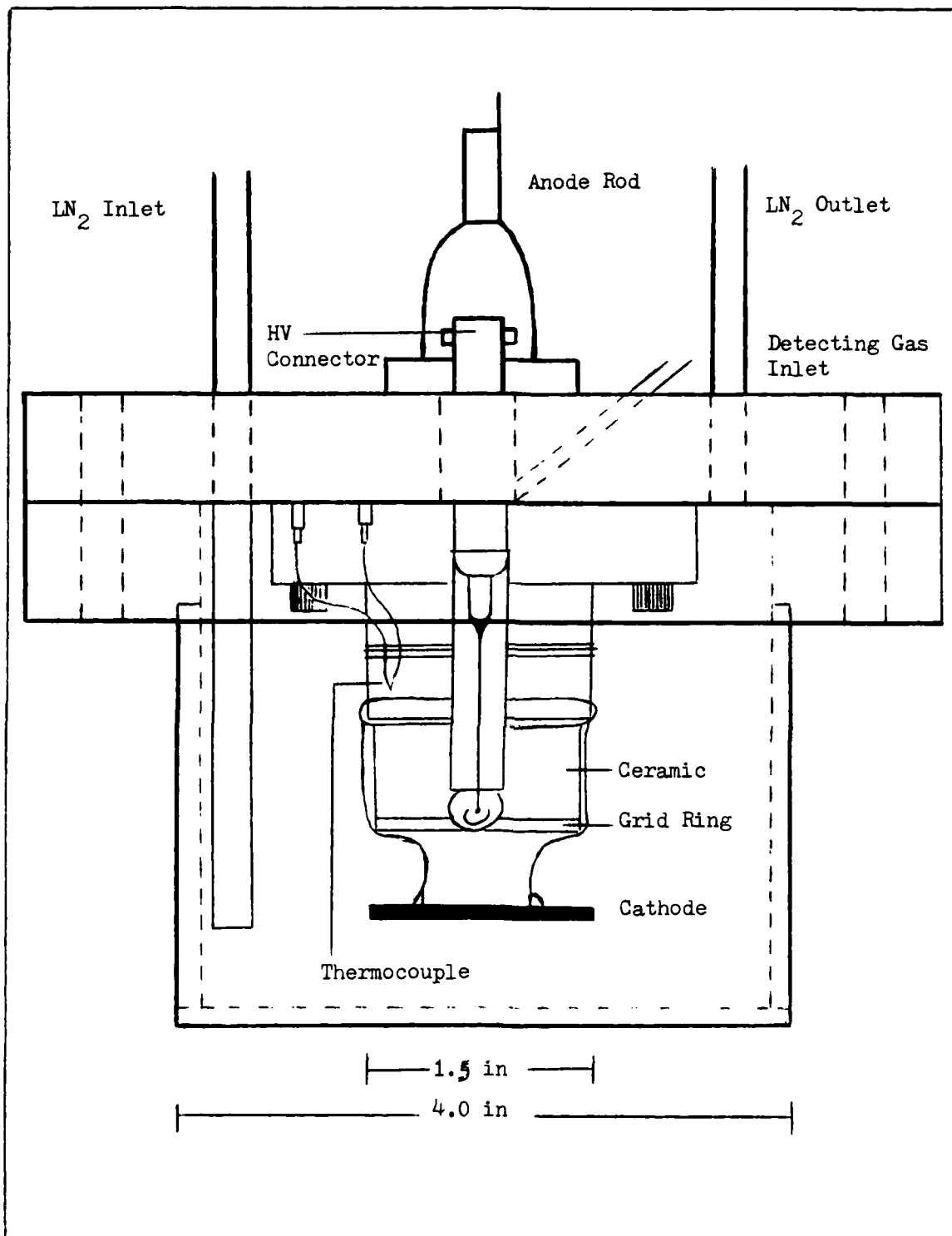


Fig. 8. The Ionization Chamber

insulated 0.25 in. copper rod which extends into the chamber. A copper plate with a threaded stem screws into the rod. The plate acts as the anode. The threaded stem allows variation of the grid to anode separation. The end of the copper rod is soldered to a wire which leads to a feedthrough for connection of a preamplifier.

The wire grid is a 0.125 in. by 0.125 in. stainless steel ring with an outer diameter of 1.25 in. The 2 mil stainless steel wires are soldered to the ring. Their separation center to center is 0.015 in. In order to decrease the cathode to grid separation a copper cylinder was placed in the bottom cylinder of the chamber. The grid to cathode distance with the copper cylinder is 0.7 cm. The grid to anode distance is 0.55 cm. These dimensions impose a ratio of the allowed electric fields. The ratio of the cathode to grid electric field to the grid to anode electric field is 0.409.

Resting on top of the grid ring is a ceramic cylinder. A 0.75 in. hole runs down the center of the cylinder allowing the anode to pass through. The ceramic helps shield the anode from the sharp edges of the grid ring. The sharp edges may act as potential discharge points.

Surrounding the whole chamber is a stainless steel bucket. This bucket is welded to a ConFlat flange which is bolted to the blank flange. The bucket provides a container for the liquid nitrogen used to cool the chamber. The whole assembly rests in an outer bucket which is evacuated. The vacuum provides insulation for the liquid nitrogen bucket.

The Electronics. The charge collected at the anode is converted into a voltage pulse by an Ortec 142-B preamplifier. Originally an Ortec 120-5 preamplifier with cooled FET was to be used, but the preamp was defective. The signal from the preamplifier is further modified by a Canberra Model

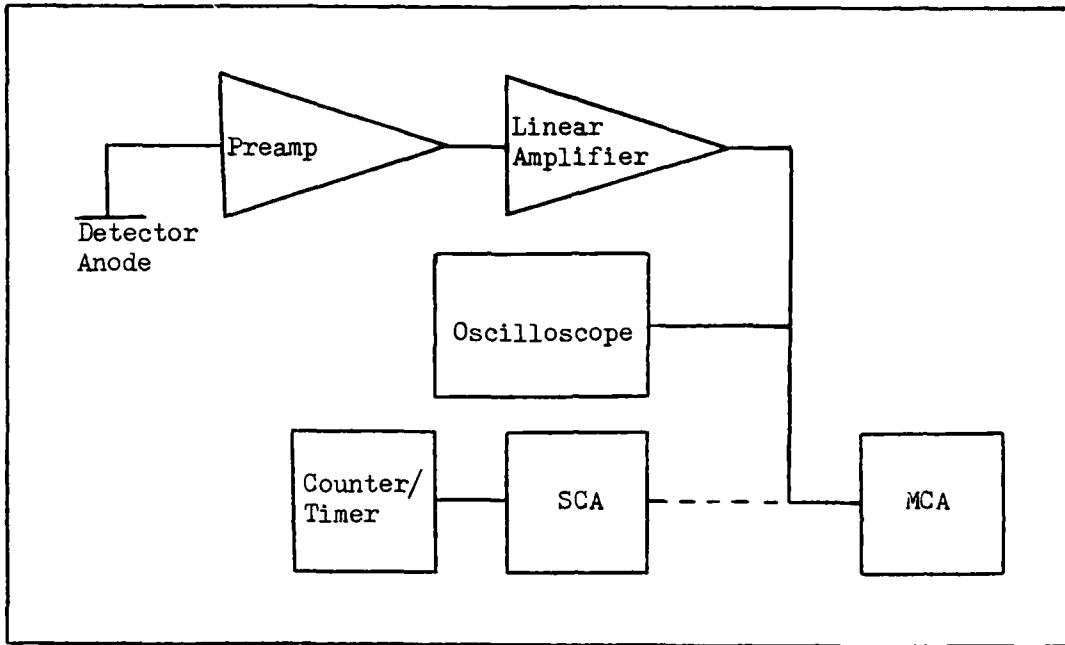


Fig. 9. The Supporting Electronics for the Ionization Chamber

2020 linear amplifier. These signals are viewed on an oscilloscope. Pulse height spectra are obtained through the use of a Nuclear Data multi-channel analyzer. A single channel analyzer and a counter/timer can replace the MCA in order to provide counts for specific areas of the spectrum.

High voltage power supplies set the grid and cathode at their negative potentials. Noise is reduced by Ortec Model 119 high voltage filters.

#### The Gas Handling System

The gas handling system is diagrammed in Figure 10. The upper system provides access to the gases used in the chamber. The purification furnace leads to the chamber itself. The outer bucket provides extra volume for gas storage and connects to the vacuum pumps.

The Purification Furnace. The purification furnace is a quartz tube

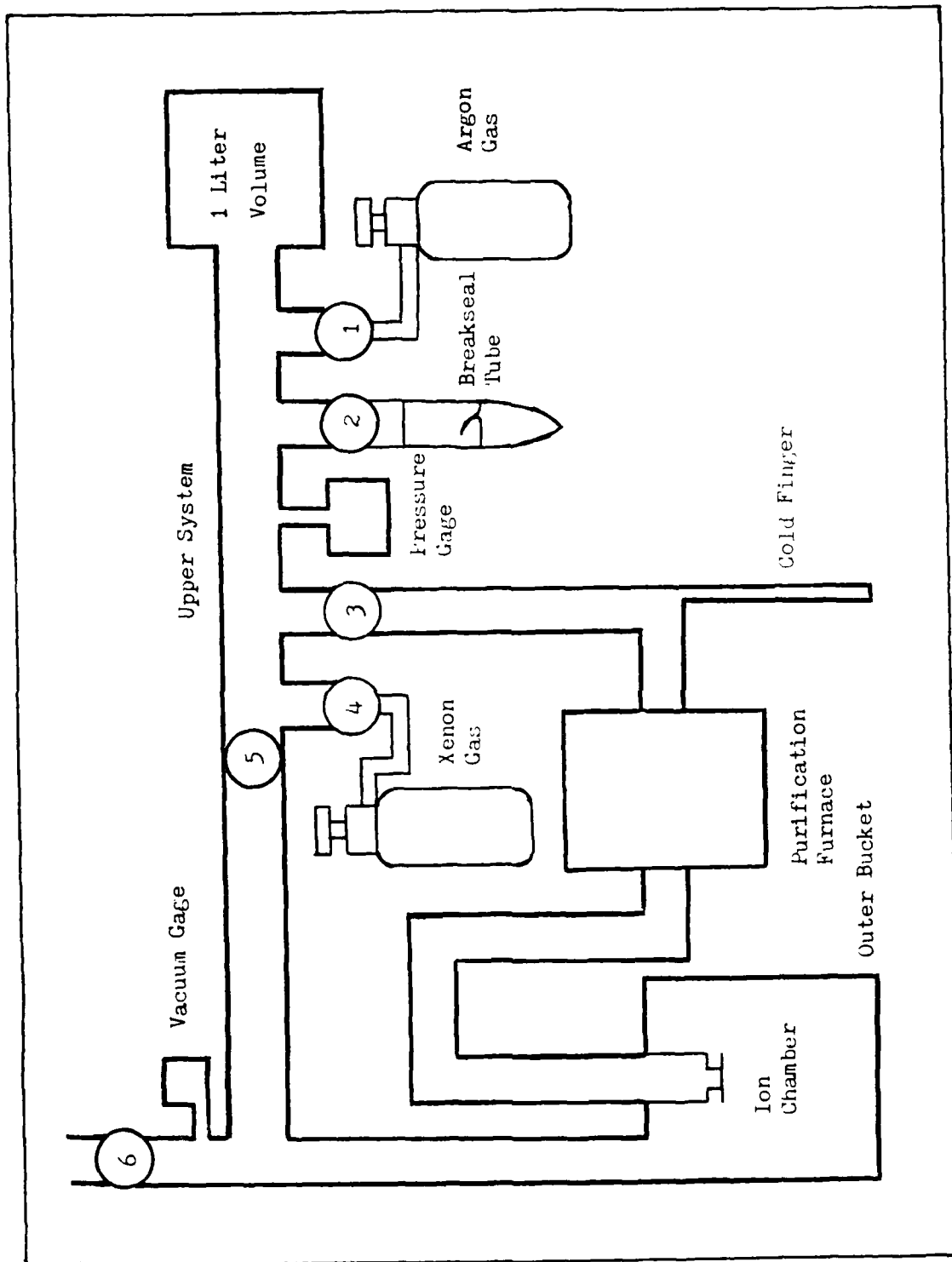


Fig. 10. The Gas Handling System

filled with turnings of titanium and zirconium. When heated to 1000 C these metals act as getters of nitrogen and oxygen. Plugs of fine copper turnings at both ends of the tube keep the titanium and zirconium in place (11). Dysprosium, which was also placed in the tube in the beginning, has a vapor pressure six orders of magnitude greater than the other metals. Signals were not observed from the chamber until after the dysprosium had been removed from the purification furnace.

One end of the tube is sealed to the noble gas inlet of the ionization chamber. The other end of the furnace is sealed to a glass adaptor. The glass adaptor is bolted to a metal "T". The "T" leads to a cold finger and valve number three. Valve three allows gas into the furnace.

The Upper System. The upper system provides a known volume for gas storage and a number of valves for gas entry. Valves 1 and 4 allow argon and xenon to enter the system from storage bottles. Valve 2 is fitted with an o-ring seal. A breakseal tube filled with a radioactive xenon sample is connected to the system here. Valve 5 connects the upper system to the outer bucket. A transducer gage permits pressure readings from 0 to 25 psi.

The Outer Bucket. The outer bucket can be evacuated as noted previously. Valve 6 leads to the vacuum system. The vacuum system consists of a roughing pump and a diffusion pump with a cold trap. A Penning Type vacuum gage is positioned in front of valve 6. The outer bucket can also be used as a large volume for gas storage.

## V Procedure

### Gas Purification

The first step in the operation of the detector involves the purification of the noble gas to be used as the detection medium. The system is prepared by allowing the diffusion pump to evacuate it overnight. The vacuum obtained is less than  $10^{-6}$  Torr. The system is then flushed with argon four times. The process is accomplished by injecting 99.999% pure argon into the system to a pressure of approximately 100 mm Hg. The system is evacuated, and the process is repeated.

After the argon flush the detecting gas is introduced into the system. The gas is injected into the outer bucket and the upper system at a pressure which allows enough gas to eventually enter the chamber. When the chamber is cooled, 2.5 ml of liquid must exist in the bottom of the chamber. Also enough gas must be present to allow the vapor pressure of the liquid to exist in the rest of the system.

The gas is brought into the purification furnace by condensing it in the cold finger. A dewar filled with liquid nitrogen is slowly raised around the cold finger. The valve to the outer bucket is then closed, and the furnace is heated to 1000 C.

After the outer bucket is evacuated, liquid nitrogen is injected into the bucket surrounding the chamber. As the chamber cools, the dewar surrounding the cold finger is lowered. The solidified gas in the cold finger boils off and diffuses through the furnace. This process is reversed and repeated two more times.

With the chamber cool and the cold finger warm, the furnace is turned

off, and the chamber is allowed to warm to the correct temperature. The correct temperature is 83 K for argon and 163 K for xenon. The temperature of the liquid is monitored by its vapor pressure. The transducer gage in the upper system is used for pressure readings. The purification process lasts an average of 11 hours.

#### Sample Introduction

The different sources under study were prepared for detection by the chamber in different manners.

Gamma Ray Exterior Sources. The gamma ray sources are encased in containers which preclude placing the sources inside the chamber. Also internal placement would not facilitate the observation of a number of different sources during one run. Therefore, the gamma ray sources are fixed to the side of the outer bucket during runs. Since the gamma photons penetrate through materials relatively well, a reasonable number of the photons still reach the detector. Calculations of the number of photons stopped in the detector are presented in Chapter VI.

Solid Interior Sources. The  $\text{Bi}^{207}$  used is plated onto the end of a small threaded metal cylinder. The copper cylinder, used in the chamber, was tapped in the center to accommodate the  $\text{Bi}^{207}$  source. The  $\text{Bi}^{207}$  rested in line with the surface of the copper cylinder. The copper cylinder was replaced in the chamber before the beginning of the purification process.

The  $\text{U}^{233}$  source is plated on a small metal punch 3 mm in diameter. Before a run the  $\text{U}^{233}$  was simply placed on top of the copper cylinder in the chamber.

Xenon-133 and Xenon-131m. An untapped copper cylinder was placed in the chamber for radioactive xenon detection. The xenon was introduced

into the system through the use of a breakseal tube. After the detection gas had been solidified in the cold finger, the breakseal was broken to allow the xenon into the system. Thus any impurities in the xenon sample would also be removed during purification.

#### Data Collection

With the gas purified and the source prepared, data collection can begin. The cathode and the grid are set at their specified potentials. The pulses from the amplifiers are analyzed. Adjustments of the gain, shaping time, or chamber potentials may be required before the signals are routed to the multi-channel analyzer.

The counting is limited since the detecting gas continually warms, and the pressure in the system rises. A rise in pressure indicates less liquid in the detecting volume of the chamber. Also high enough internal pressures can damage the glass chamber. Thus another injection of liquid nitrogen is necessary to recool the chamber. The chamber must warm again to the correct temperature before further data can be collected. After data collection is complete, the valve to the outer bucket is opened to allow expansion of the gas.

## VI Results

The data from the various sources is presented in two subsections one for the exterior sources and one for the interior sources. Some initial considerations about maximum pulse heights, xenon detecting gas and background noise are presented first.

### Initial Considerations

The maximum pulse heights for particles of a certain energy are estimated from the conversion gain of the preamplifier. The output from the preamplifier is 20 mV for a 1 MeV particle in silicon. The W value used is 3.6 eV/ip so 20 mV is generated from 277,777 ion pairs. A 1 MeV particle in argon produces 42,373 ion pairs. This would result in a 3.05 mV pulse from the preamplifier. Similar calculations are carried out for particles of different energies.

After initial results were obtained with argon and the exterior sources, xenon was introduced as the detecting gas. No significant results were obtained with xenon in four runs. It is assumed that the higher density of xenon increased recombination effects. Although signals may have been detected for the higher energy electrons of Bi<sup>207</sup>, it was decided to stay with argon. The energy of the radioactive xenon emissions are not as high energy as those of Bi<sup>207</sup>, and xenon isotope detection is the main purpose of the chamber.

The background observed without sources present was negligible. It was less than one count per second as long as the voltage was kept below the discharge point. Noise was still observed at the low energy end of some of the spectra. The ions diffusing through the gas may have acted

to induce some small discharges. Magnitudes of breakdown voltages in the gas are calculated in the appendix. Discharges did appear for electric fields in the gas between 4.0 kV/cm and 6.0 kV/cm.

#### The Exterior Sources

Electron Mobility. The  $\text{Am}^{241}$  source displayed the most distinguishable peak of the exterior sources. This occurred because of its high activity. Also the detector has a relatively high efficiency for the 59.96 keV gammas emitted by the source.

$\text{Am}^{241}$  provided electron mobility data in liquid argon. The pulse height spectra of  $\text{Am}^{241}$  for a grid to cathode electric field of 2.447 kV/cm are shown in Figure 11. The different spectra illustrate the effect of different linear amplifier shaping times on the magnitude of the voltage pulses. The pulse heights are maximized with a shaping time of 6  $\mu\text{s}$ .

The peak of the pulse heights with a 6  $\mu\text{s}$  shaping time represents an electron collection time of 6  $\mu\text{s}$ . The electrons pass through 0.7 cm of liquid argon and 0.55 cm of gaseous argon. The transit time through the gas is 0.13  $\mu\text{s}$  given a drift velocity of  $4.2 \times 10^6$  cm/s (24:59). The electron drift time in the liquid is thus 5.87  $\mu\text{s}$  implying a drift velocity of  $1.2 \times 10^5$  cm/s. The value reported by Shibamura at this electric field is approximately  $2.5 \times 10^5$  cm/s (25:254).

Activity. Theoretical count rates reported by the detector for the different sources have been calculated and compared to the actual measured counts. The sources are placed on the side of the outer bucket 10.2 cm from the chamber in line with the chamber bottom. The cross sectional area of the chamber is  $1.4 \text{ cm}^2$ . For the purpose of calculating the geometry fraction, the area is considered to be a circle. With these values the geometry fraction,  $f_g$ , is  $1.08 \times 10^{-3}$ .

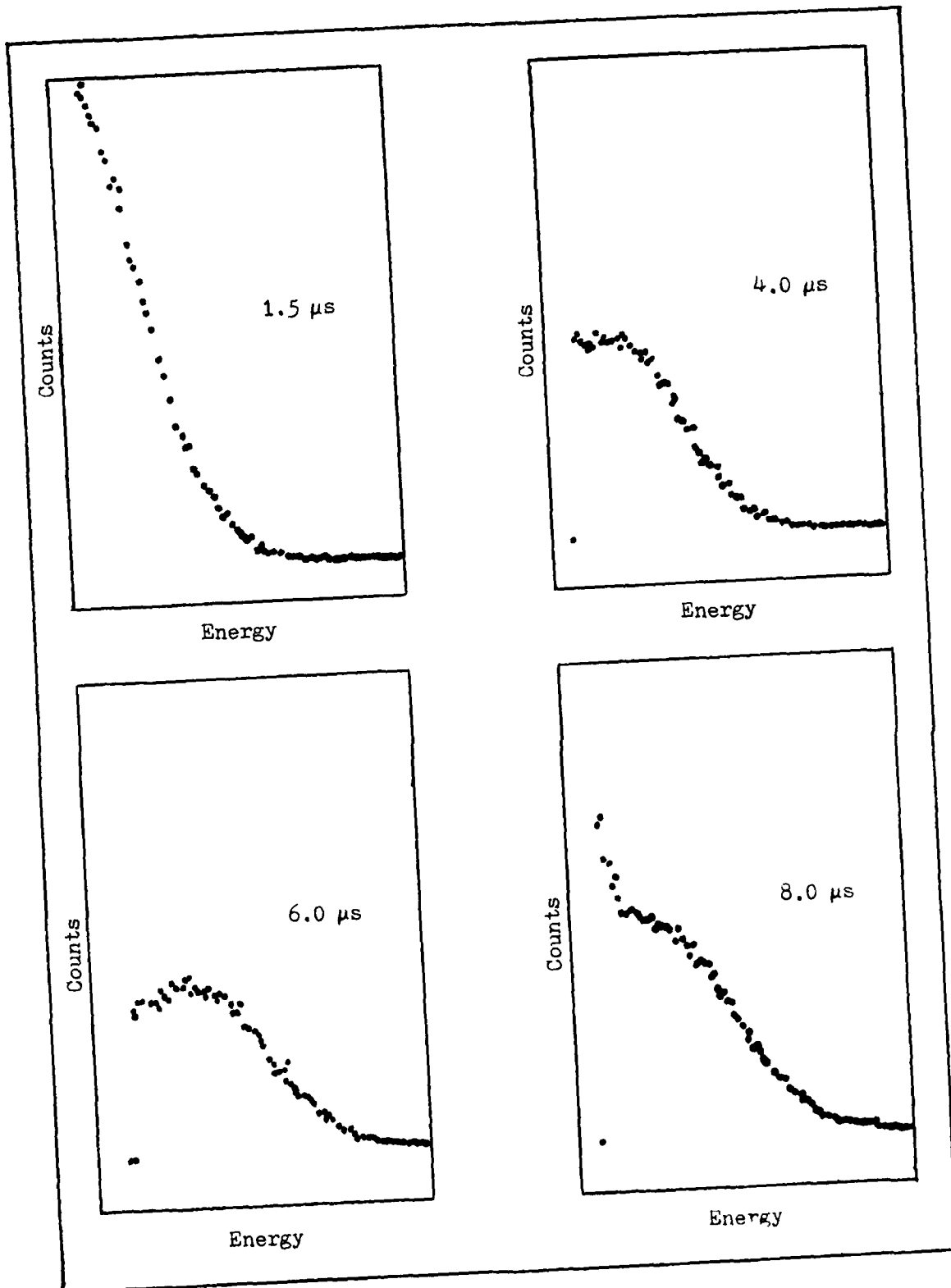


Fig. 11. Americium-241 Electron Drift Velocity Study

TABLE VI

## The Efficiency Fractions

Source	Photon Energy keV	$f_{ab}$	$f_{s}^{\text{Photons}}$	$f_{s}^{\text{Electrons}}$	$f_b$
Am <sup>241</sup>	59.96	0.0422	0.530	0.994	0.359
Cd <sup>109</sup>	88.03	0.278	0.200	0.991	0.0361
Co <sup>57</sup>	123.0	0.478	0.0913	0.990	0.962

The scattering and absorption of photons before they reach the chamber must be considered for a 0.34 cm thickness of stainless steel. The calculated absorption fractions are listed in Table VI. These were calculated using the mass attenuation coefficients of iron.

The fraction of photons stopped by 1.6 cm of argon then affects the intrinsic efficiency of the detector. Since the photons are stopped throughout the volume of the chamber, the fraction of scattered electrons which are subsequently stopped must also be considered. The last column in the table lists the branching fractions of the radionuclides for the photons which are detected by the chamber. The listing for Co<sup>57</sup> is an average of the 122 keV and 136 keV photons.

In Table VII the theoretical number of photons which reach the chamber, the theoretical number of photons stopped in the chamber, and the actual measured number of counts are listed. The intrinsic efficiencies of the chamber for the photons of energies from 60 keV to 136 keV range from 70% to 7.2%.

The measured counting rates differ from the theoretical values by 20% to 30%. Because of the assumptions in the theoretical values, these percentages are reasonable. The photopeaks observed were also partially

TABLE VII

## The Yray Source Counting Rates

Source	Activity ( $\mu\text{Ci}$ )	Theoretical # Reaching the Chamber	Theoretical Counts per Second	Actual Counts per Second
$\text{Am}^{241}$	294	178	94	125
$\text{Cd}^{109}$	$62.4 \pm 10\%$	25	5.0	3.5
$\text{Co}^{57}$	$8.95 \pm 4.4\%$	164	15	12

cut off on the lower energy side due to limitations of the linear amplifier gain. The linear amplifier gain was set at its maximum value of 3900 for these spectra.

The spectra for the gamma sources also illustrate the minimum counting rate necessary for reasonable energy resolution with this detector. The  $\text{Cd}^{109}$  and  $\text{Co}^{57}$  spectra in Figure 12 show the resolution for low count rates. All of the spectra are for counting times of 200 s.

The counting times are limited to 30 min or less because of the constant vaporization of the liquid argon. The argon must then be re-cooled and liquified in the chamber bottom. After this process a degradation in amplitude and fwhm of the energy peaks was observed. Therefore, for the system in its present form count rates on the order of 5 cps or greater are needed.

Pulse Height vs E-field. A study of pulse height versus electric field is presented in Figure 13. The pulse heights are listed as the observed voltage,  $V$ , divided by the theoretical maximum voltage,  $V_0$ , of the pulses for the combined 122 keV and 136 keV peaks of  $\text{Co}^{57}$ . The theoretical curve is based on equation (18) with an impurity concentration

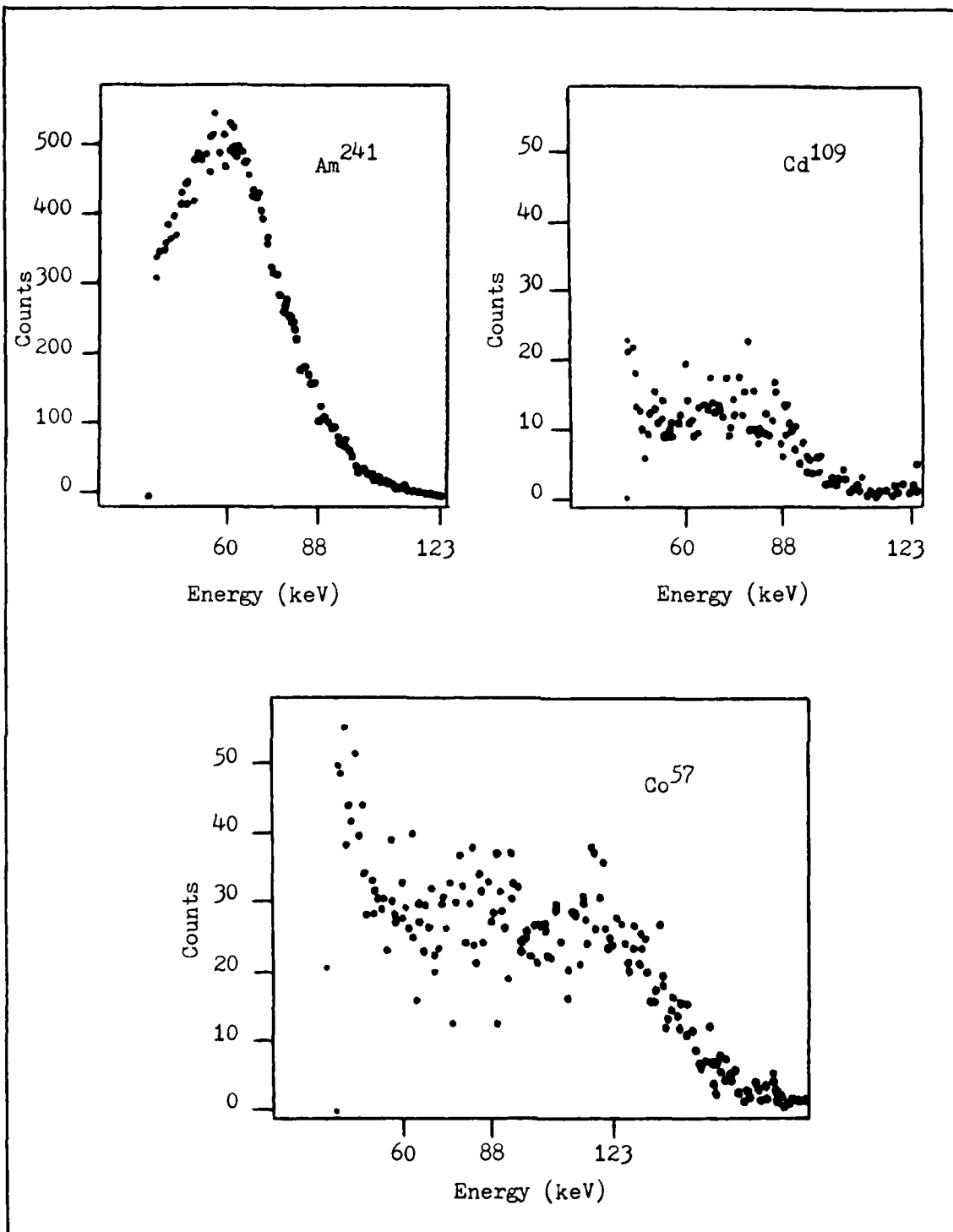


Fig. 12. The  $\gamma$ ray Sources Energy Spectra

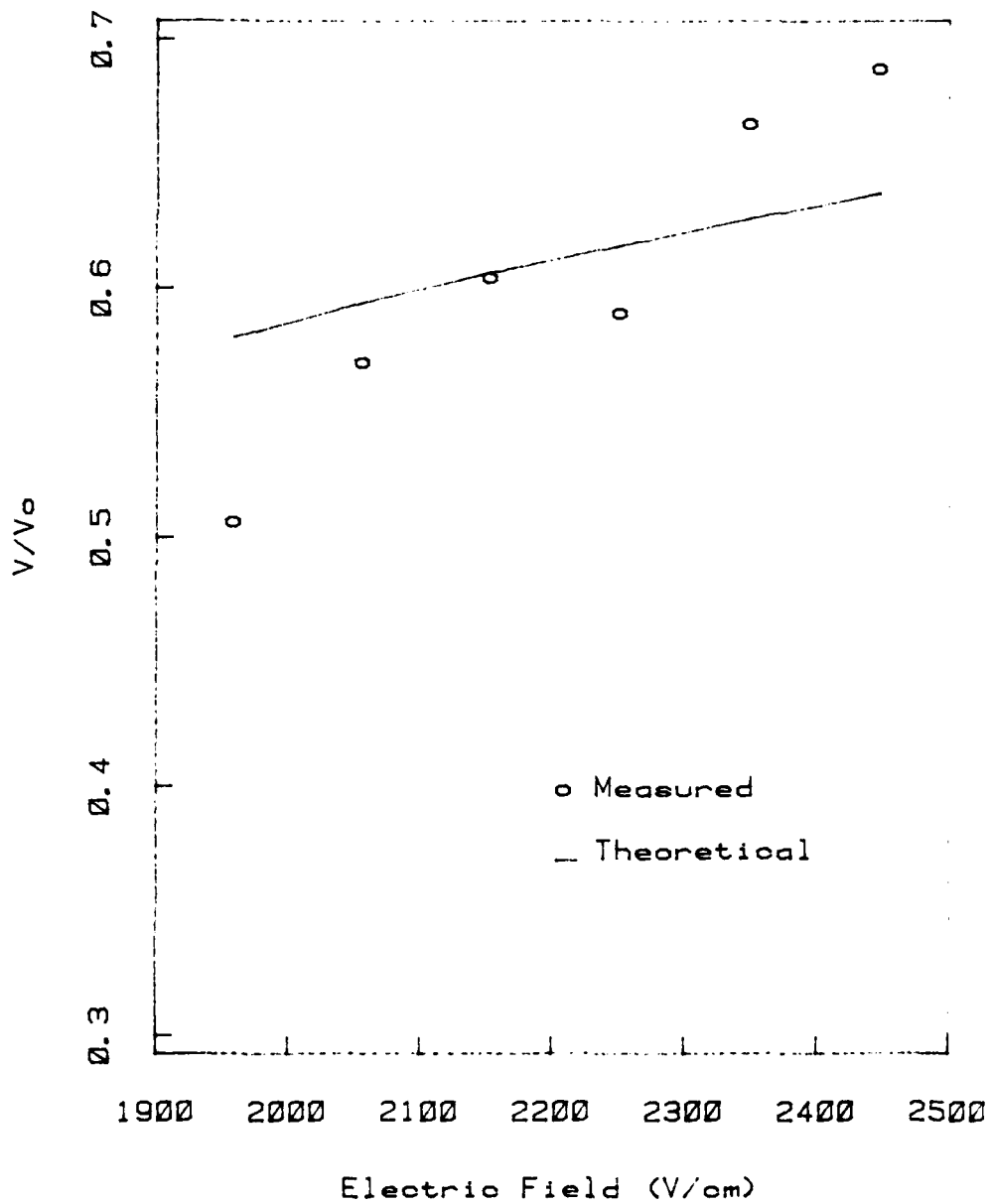


Fig. 13. Pulse Height vs Electric Field (Co-57)

of 0.8 ppm calculated from the  $V/V_0$  value at an electric field of 2.153 kV/cm.

The greater slope of the measured curve may be due to uncertainties in the magnitude of the peaks measured for  $\text{Co}^{57}$ . The number of counts recorded was low, and the peaks were not far above the noise level in the system.

Resolution. The energy resolution of the  $\text{Am}^{241}$  peak is 29 keV for the 59.9 keV peak. The full width at half maximum of a test pulse set to a corresponding voltage is 11.5 keV. The energy resolution for the argon without noise can be approximated by

$$\text{fwhm}_A = (\text{fwhm}_t^2 - \text{fwhm}_p^2)^{1/2} \quad (25)$$

where

$\text{fwhm}_t$  is the total resolution

$\text{fwhm}_p$  is the test pulse resolution

The measured resolution for liquid argon is thus 27 keV fwhm or 45% for a 60 keV peak. This resolution is not good enough to make this system a useful substitute for liquid scintillators.

### Interior Sources

Bismuth-207. The high energy internal conversion electrons of  $\text{Bi}^{207}$  allowed a study of chamber characteristics further above the background noise inherent in the system. The activity of this source is  $0.227 \mu\text{Ci}$  as determined with a  $\text{Ge}(\text{Li})$  detector. The branching fraction for the 1.064 MeV transition is 0.88. This is further modified by an internal conversion electron to gamma ratio of 0.115. The geometry factor with the  $\text{Bi}^{207}$  on the cathode is 0.5. Since the range of the electrons is 0.31 cm, those emitted onto the chamber are presumed to be stopped.

Thus the expected count rate for the internal conversion electrons from the 1.064 MeV transition is 425 cps. The measured count rate is 332 cps. The measured value is low by 22%. The large fwhm of the peak leads to uncertainties in the actual number of counts under the peak. The efficiency for the 1.064 MeV electrons is 39%.

The mobility study with  $\text{Bi}^{207}$  resulted in a different value for the electron drift velocity. The maximum magnitude for pulse heights was obtained with a shaping time of  $4 \mu\text{s}$ . With an electron transit time through the gas of  $0.13 \mu\text{s}$ , the transit time through the liquid is  $3.87 \mu\text{s}$ . The drift velocity thus has a value of  $2.58 \times 10^5 \text{ cm/s}$ . This value agrees closely with that obtained by Shibamura.

In Figure 14 a second study of pulse height versus electric field is shown. In this case the measured values appear to correspond more closely to the theoretical curve. The theoretical curve is a fit for an impurity level of 1.3 ppm  $\text{O}_2$ . Such fluctuations in impurity levels are possible since the purification process is not exactly repeatable for every run.

One feature of the gridded ion chamber is the decrease of the signal

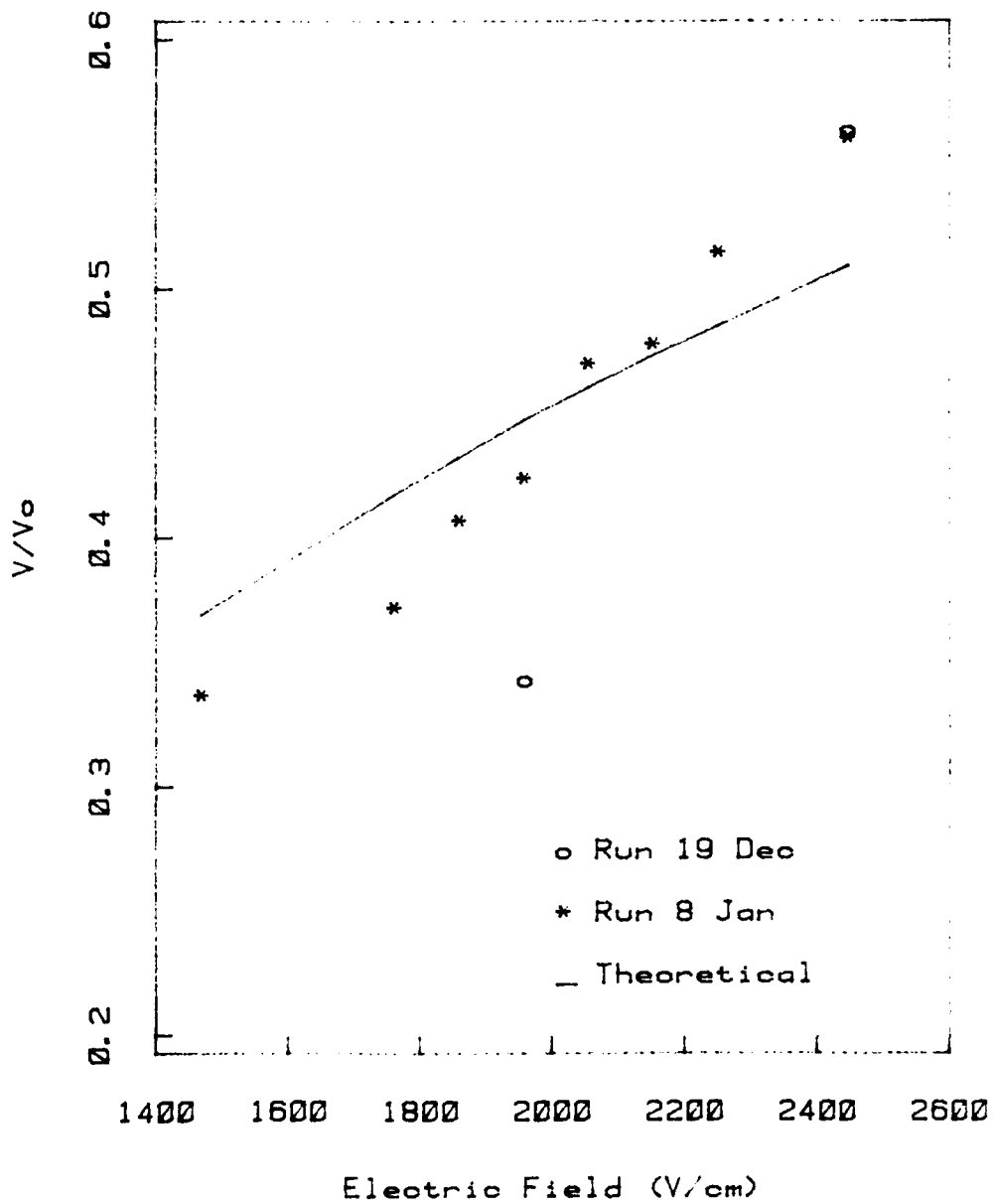


Fig. 14. Pulse Height vs Electric Field (Bi-207)

if the electric field between the grid and the cathode,  $E_c$ , becomes too large in comparison to the electric field between the grid and the anode,  $E_a$ . This causes a violation of equation (9), and electrons begin to collect on the grid. A theoretical measure of this decrease of the signal in relation to the electric field ratio has been calculated by Bunemann (5:197-198). The curve appropriate for the grid dimensions used in this study is shown in Figure 15.

The experimental values were obtained by holding  $E_c$  constant and varying  $E_a$ . In this way recombination effects in the liquid did not interfere with the results. The signals measured are 5% to 8% smaller than they should be, but they follow the theoretical curve fairly close. Bends in the wires or other grid imperfections could have caused the loss in signal voltage. This data indicates that the gridded chamber is functioning according to theory.

A study of pulse height with a change in grid voltage is shown in Figure 16. The channel of the peak recorded by the MCA does not change significantly. As mentioned above, the decrease of the grid voltage tends to decrease the magnitude of the voltage pulses. Opposing this is the increase of the voltage pulses due to a larger electric field across the liquid argon.

These spectra show an increase in energy resolution. The visible peak is a combination of the 0.975 MeV and 1.050 MeV internal conversion electron peaks. Further decreases of the grid voltage lead to loss of signal magnitude and energy resolution. The energy resolution of the peak for a chamber electric field of 2447 V/cm is 430 keV fwhm or 43%. This resolution is comparable to that obtained with  $\text{Am}^{241}$ . The resolution for the highest electric field of 3429 V/cm is 172 keV fwhm or 17%. These

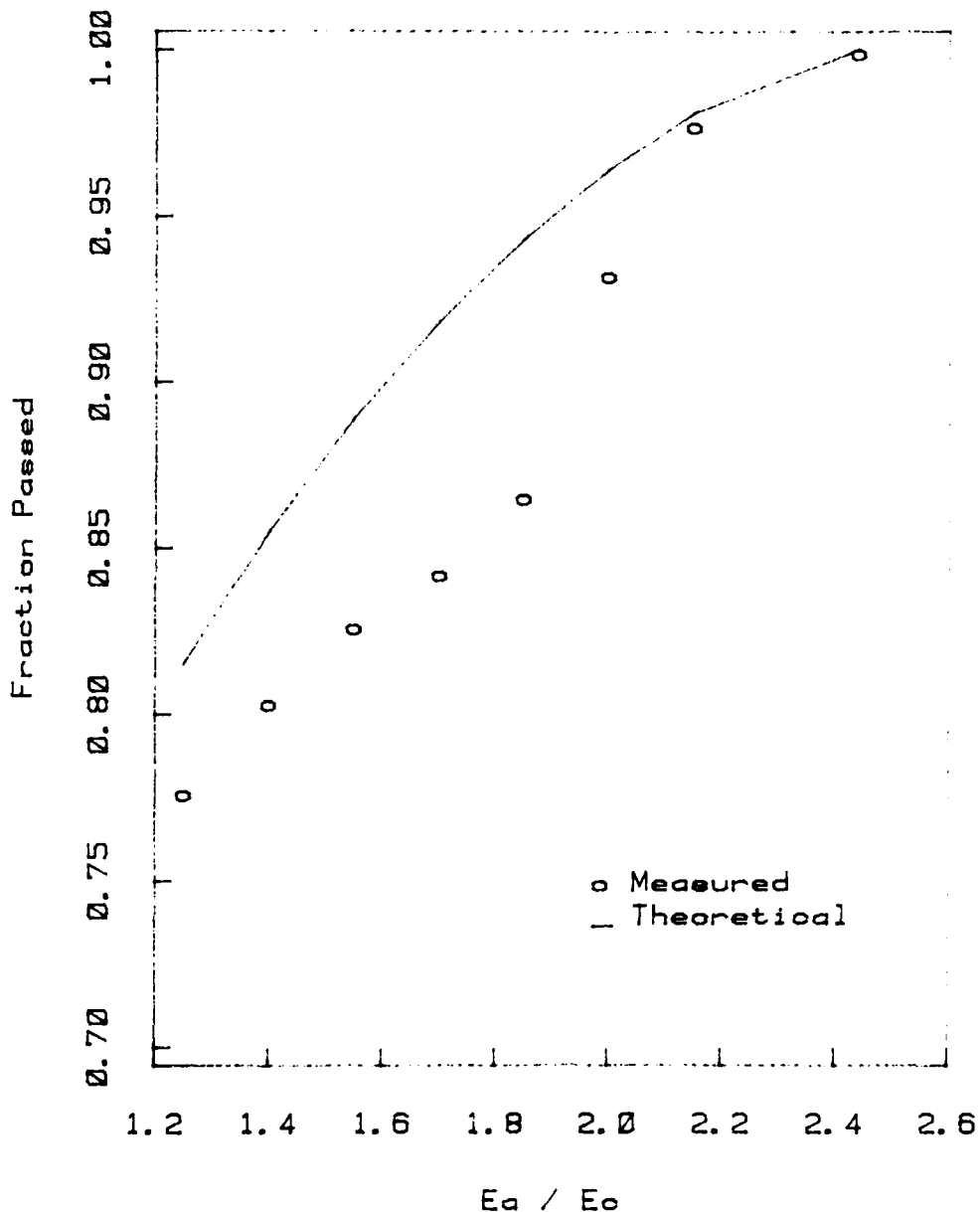


Fig. 15. Fraction of Electrons Passed vs  $E_a/E_0$

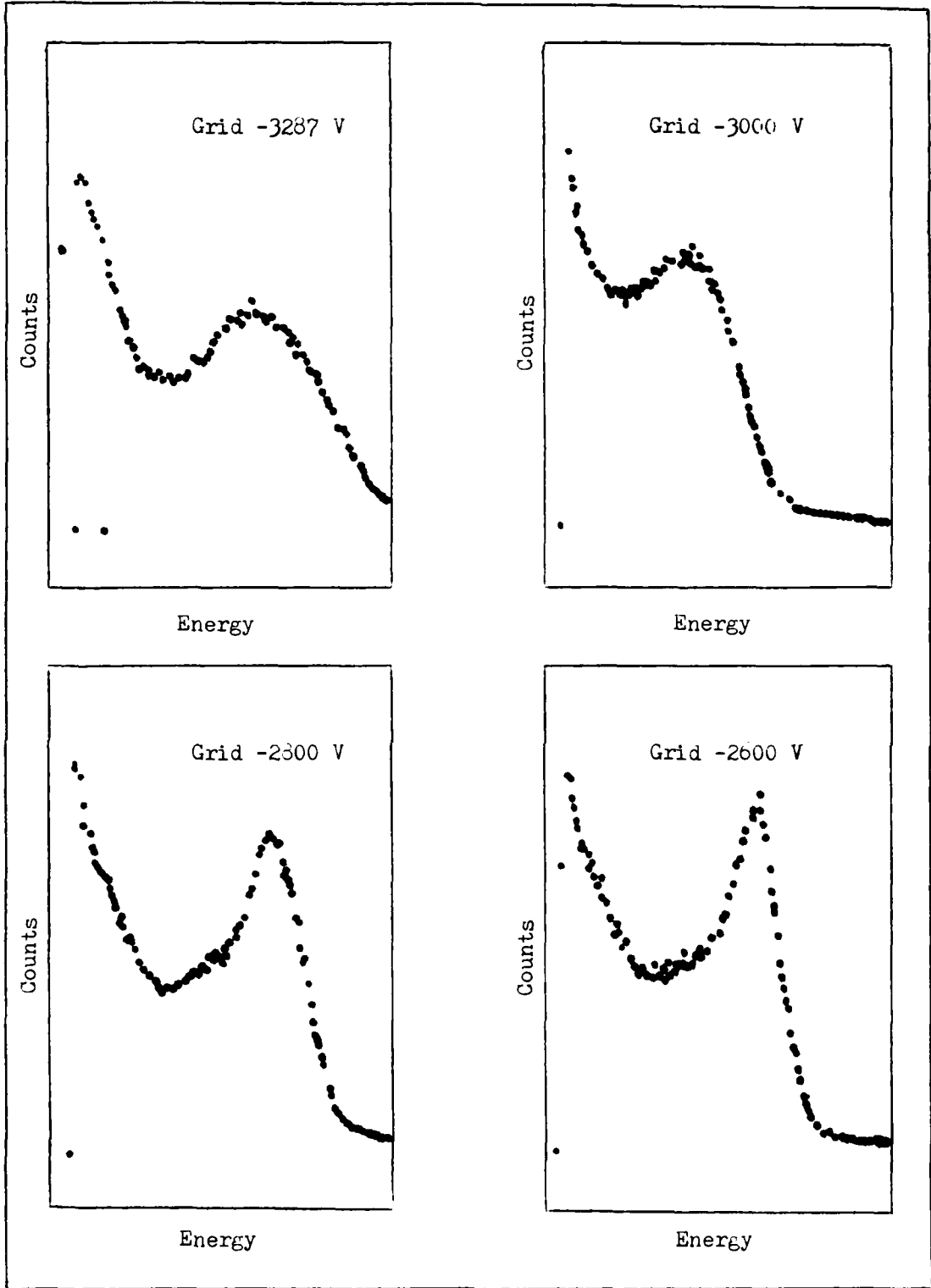


Fig. 16. Decrease in Grid Voltage with -5.0 kV on the Cathode

resolutions are poor enough to combine pulses from electrons of the two different energies into one peak.

These peaks have been distinguished by Shibamura with an energy resolution of 34 keV fwhm as shown in Chapter II. Also shown in Chapter II is the Bi<sup>207</sup> spectrum obtained with an electric field of 5.5 kV/cm and an electrode separation of 1.43 cm. The resolution obtained in this study lies between these two extremes. These three studies illustrate the characteristics needed in a liquid noble gas ionization chamber for accurate energy resolution. The electric field across the liquid must exceed 10 kV/cm. The impurity concentration must be around 1 ppm O<sub>2</sub>. The distance traveled by ion pairs through the liquid must be minimized.

Uranium-233. The 4.82 MeV alpha peak from U<sup>233</sup> is shown in Figure 17. A number of the alpha decays leave Th<sup>229</sup> in excited states. These deexcitations may be the cause for the number counts to the left of the peak. The magnitude of the peak corresponds to an energy of 634 keV for a beta particle. Initial recombination caused by the greater track density for the alpha particles has reduced the peak 87%. The resolution of the peak is 103 keV fwhm using the calibration obtained with internal conversion and photoelectric electrons. On the scale for alpha particles the resolution should be 793 keV fwhm or 16.4%.

The shorter ion pair tracks of the alpha particles have resulted in a loss of signal magnitude compared with the less dense beta type tracks. On the other hand, the shorter tracks have decreased the difference in length of the paths which the electrons of different tracks must travel through the liquid. The electron attachment effect is less dependent on the initial direction of the track, and as expected the energy resolution has improved. So for better energy resolution the effects of volume

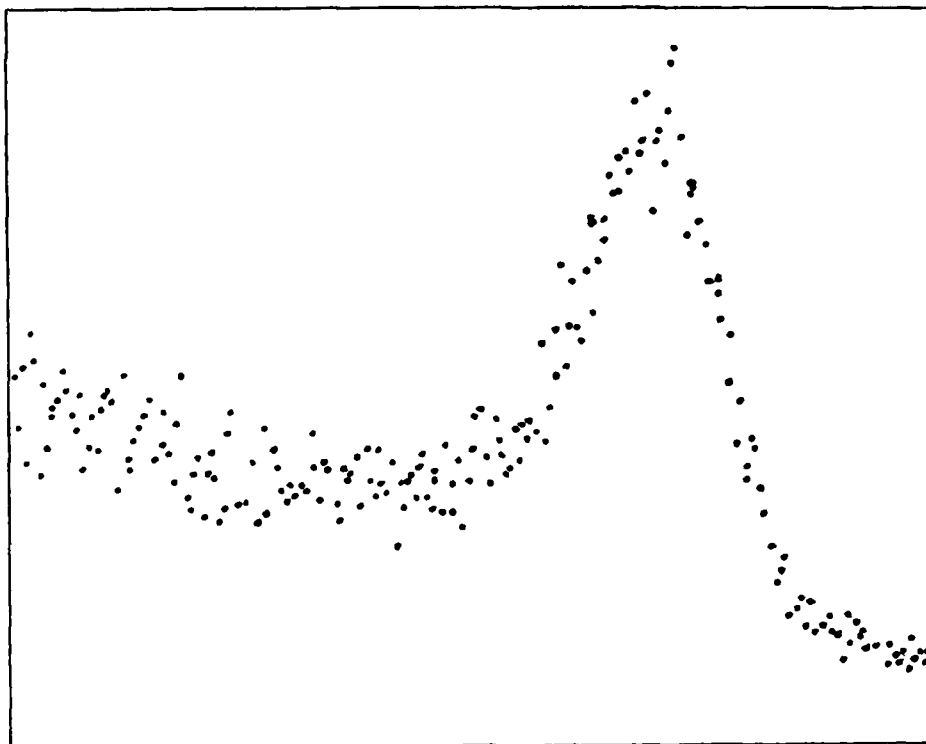


Fig. 17. The Uranium-233 4.82 MeV Alpha Peak

electron attachment must be reduced.

Xenon-131m and Xenon-133. The results of the differentiation between  $\text{Xe}^{131\text{m}}$  and  $\text{Xe}^{133}$  are inconclusive. The energy spectrum of a combined sample of the two nuclides is presented in Figure 18. The shape of the plot indicates a beta spectrum, but no peak corresponding to the 164 keV decay of  $\text{Xe}^{131\text{m}}$  is visible. Due to the poor energy resolution of the system and the activity ratios, the 164 keV peak may not be large enough to distinguish. The peak could be distinguished by allowing further decay of the sample. Since the  $\text{Xe}^{133}$  decays faster, the 164 keV peak would eventually show above the beta spectrum.

The spectrum ends near 400 keV. With an energy resolution around 40% the 346 keV maximum of the actual beta spectrum falls within the error

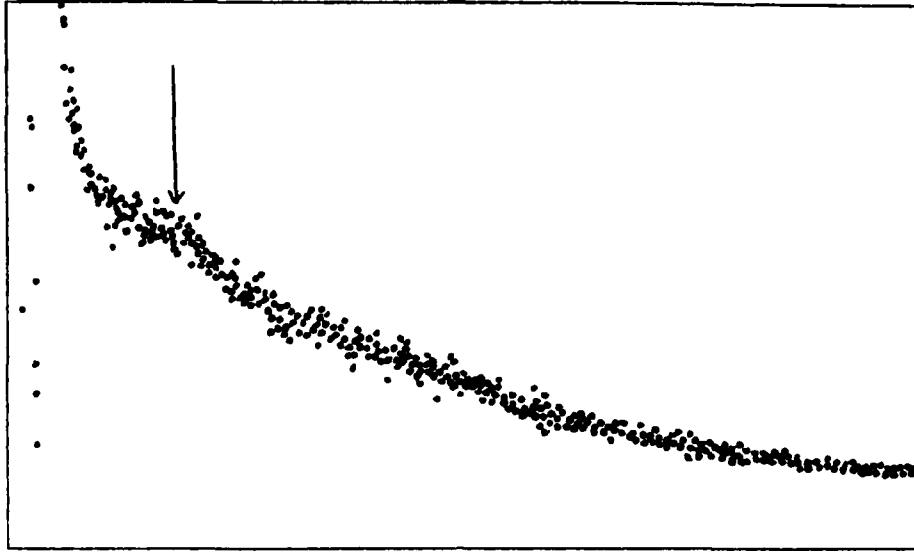


Fig. 18. The Xenon-131m and Xenon-133 Combined Spectrum

limits of the measured maximum. The small discontinuity at the low energy end of the spectrum occurs at 200 keV. This may be partially caused by the  $\text{Xe}^{131\text{m}}$  internal conversion electrons.

The count rate observed for the sample was 365 cps. This not the activity of the total sample since part of the xenon exists in vapor form throughout the rest of the system. The system is not useful for the measurement of the total activity of a radioactive xenon sample.

## VII Conclusions and Recommendations

### Conclusions

The detecting system in its present form does not achieve the goal of differentiating the radioisotopes of  $\text{Xe}^{131\text{m}}$  and  $\text{Xe}^{133}$ . They may be differentiated by allowing the decay of the isotopes until the  $\text{Xe}^{131\text{m}}$  peak is visible. Even so the energy resolution of the system is about 45% for energies of interest. This is not much better than liquid scintillators. The effort spent to run the system is also a drawback.

The different sources studied provide information on the characteristics of the chamber. The intrinsic efficiency of the chamber has a maximum of 70% for 60 keV  $\gamma$ rays. The efficiency decreases to 7.2% for  $\gamma$ rays of 122 keV. The resolution at these energies is 48% with 11.5 keV fwhm caused by noise from the preamplifier.

The higher energy internal conversion electrons from  $\text{Bi}^{207}$  exhibit resolutions of 43%. A decrease in the grid voltage improves resolution at the expense of voltage pulse magnitude. The efficiency for a source set on the cathode is 39%. A volume distribution of the source could lead to efficiencies of 80% as shown by  $\text{Am}^{241}$ . This was not proven with the xenon samples. On the whole the detector does exhibit high efficiency properties, but high energy resolution has not been attained.

Electron attachment throughout the liquid volume of the chamber is the most likely cause of the poor resolution. The influence of electron attachment can be decreased by changing two parameters of the system. The electric field across the liquid can be increased, or the electro-negative impurity concentration in the liquid can be decreased.

Both alternatives present difficulties. In the present chamber set-up an increase in electric field will cause more noise in the system because of discharges. These discharges occur through the vapor between the grid and the anode. A decrease in impurity concentration would require a lengthening of the purification process. The present purification time puts a strain on the experimenter. There may be methods to solve these problems.

#### Recommendations

Purification System. The purification process can be improved by designing an automatic system. In this way the experimenter could let it function overnight, and the system would be ready to run in the morning. This would result in faster turn around times for the study of different internal sources.

The basic design of such a purification furnace is simply a high pressure bottle. The titanium and zirconium turnings are placed in the bottle, and the detecting gas is injected into the bottle for purification. The increase in pressure due to the heating of the gas would not affect the bottle. The bottle could be connected at one of the valves presently on the system. The connecting tube should be made of glass to insulate the system from the hot bottle.

The bottle could be heated to lower temperatures than the present system and still achieve greater purification. All of the gas would be inside the furnace during the whole procedure, and the purification would be carried out for a longer time. Also during purification the rest of the system would still be evacuated. This proposal is similar to the system used by Shibamura, et al for their noble gas chamber (25).

The Present Chamber. Changes in the present detector could also

improve resolution. The preamplifier should be replaced with one of lower noise. The Ortec 120-5 preamplifier with a FET attached to the cooled part of the system may have fulfilled this requirement, but it did not function properly.

The grid voltage could be set at values below those determined by the Bunemann equations. This would increase the electric field in the liquid. With a lower noise preamplifier the gain of the system could be increased to offset the decrease in pulse amplitude.

Proportional Counter. A liquid noble gas proportional counter could be constructed. With this counter only liquid would be in the chamber. Higher electric fields could be obtained without causing discharges. The question remains whether multiplication and high energy resolution could be achieved with such a chamber (3:36). A possible design for the chamber appears in Figure 19.

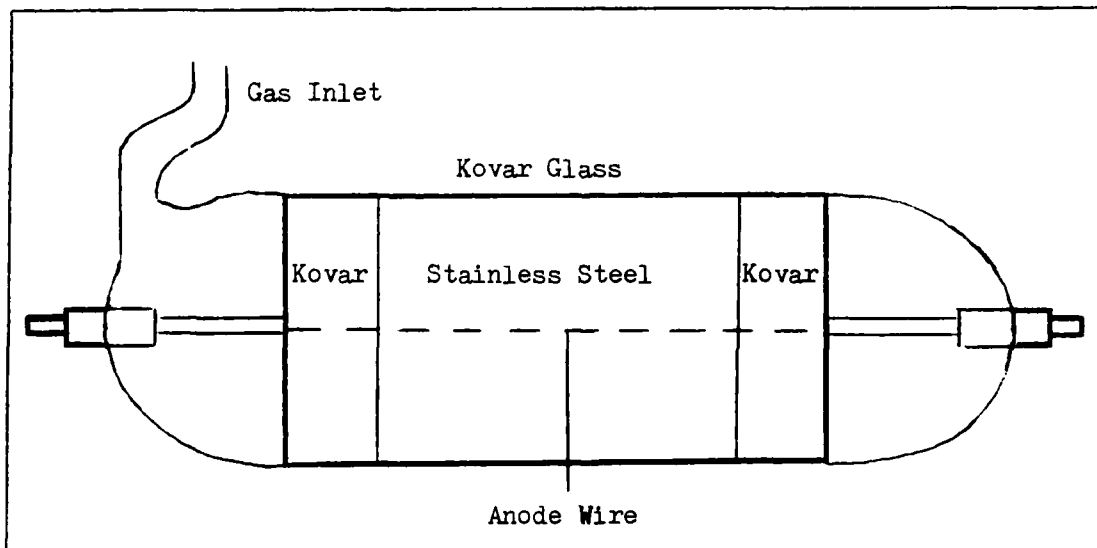


Fig. 19. A Liquid Noble Gas Proportional Counter

The center of the tube is stainless steel with kovar tubes silver soldered to the ends. Kovar glass end caps are sealed to the kovar metal. Hypodermic needles in the end caps act as holders for the anode wire. Smaller hypodermic needles are soldered to the wire on the inside to prevent multiplication outside of the uniform electric field region. The smaller hypodermic needles are then soldered to the needles in the end caps. The glass inlet tube can extend from an end cap to a 1.5 in. diameter flange. This flange can be connected to the present system.

With a cathode radius of 0.3 cm and an anode radius of  $7.62 \times 10^{-4}$  cm a 5000 V potential at the cathode provides substantial electric fields in the chamber. The electric field at the cathode is 2.8 kV/cm. The electric field at the anode surface is 1100 kV/cm.

The preceding proposals may or may not provide the energy resolutions required. Many of the problems occur because of a need for high energy resolution with a volume distributed source of low activity. A study completed in this laboratory with a high pressure noble gas proportional counter appears to have more promising results (18).

## Bibliography

1. Andrews, W. L. "Evaluation of a Detection System Employing Two Silicon Semiconductors for the Analysis of Radioactive Noble Gases," Unpublished thesis. School of Engineering, Air Force Institute of Technology, Wright-Patterson AFB, OH, March 1982.
2. Berggren, S. R. "A Cryogenic Argon Ionization Chamber Detector for Analysis of Radioactive Noble Gases," Unpublished thesis. School of Engineering, Air Force Institute of Technology, Wright-Patterson AFB, OH, March 1982.
3. Brassard, C. "Liquid Ionization Detectors," Nuclear Instruments and Methods, 162: 29-47 (1979).
4. Brodsky, A. B. Handbook of Radiation Measurement and Protection. West Palm Beach: CRC Press, 1978.
5. Bunemann, O. et al. "Design of Grid Ionization Chambers," Canadian Journal of Research, 27 (A): 191-205 (1949).
6. Chitwood, R. B. "Production of Noble Gases by Nuclear Fission," page 76 in Proceedings of the Noble Gas Symposium, ERDA CONF-730915, Stanley, R. E. and Moghissi, A. A., Editors, 1974.
7. Condon and Odishaw. Handbook of Physics. New York: McGraw-Hill, 1958.
8. Doke, T., et al. "Estimation of Fano Factors in Liquid Argon, Krypton, Xenon, and Xenon-Doped Liquid Argon," Nuclear Instruments and Methods, 134: 353-357 (1976).
9. Edmiston, M. D. and Gruhn, C. R. "Energy Resolution Considerations in Liquid Ionization Chambers," IEEE Transactions on Nuclear Science, NS-25 (1): 352-353 (February 1978).
10. Francis, Gordon. Ionization Phenomena in Gases. New York: Academic Press Inc., 1960.
11. Gibbs, D. S. et al. "Purification of the Rare Gases," Industrial and Engineering Chemistry, 48 (2): 289-296 (February 1956).
12. Gruhn, C. R. and Loveman, R. "A Review of the Physical Properties of Liquid Ionization Chamber Media," IEEE Transactions on Nuclear Science, NS-26 (1): 110-119 (February 1979).
13. Hallett, A. C. "Liquid- and Solid-State Properties" in Argon, Helium, and the Rare Gases, Volume 1, edited by Gerhard A. Cook. New York: Interscience Publishers, 1961.

14. Hampel, C. A., Editor. The Encyclopedia of the Chemical Elements. New York: Reinhold Book Corporation, 1968.
15. Hofmann, W., et al. "Production and Transport of Conduction Electrons in a Liquid Argon Ionization Chamber," Nuclear Instruments and Methods, 135: 151-156 (1976).
16. Huffman, W. A., et al. "Recent Results in the Development of Liquid Argon Imaging Chambers," IEEE Transactions on Nuclear Science, NS-26 (1): 64-67 (February 1979).
17. Knoll, Glenn F. Radiation Detection and Measurement. New York: John Wiley and Sons, 1979.
18. Lackey, R. "A High Pressure Noble Gas Proportional Counter for Analysis of Radioactive Noble Gases," Unpublished thesis. School of Engineering, Air Force Institute of Technology, Wright-Patterson AFB, OH, May 1984.
19. Lederer, M. C., et al. Table of Isotopes (Sixth Edition). New York: John Wiley and Sons Inc., 1967.
20. Meek, M. E. and B. F. Rider. "Compilation of Fission Product Yields," Vallecitos Nuclear Center, ORNL-TM-3515, August 1971.
21. McMaster, W. H., et al. Compilation of X-ray Cross Sections. UCRL-50174 Sec. II, Rev. 1. Livermore: Lawrence Radiation Laboratory, University of California, 1969.
22. Moses, A. J. The Practicing Scientist's Handbook. New York: Van Nostrand Reinhold Co., 1978.
23. Papoular, R. Electrical Phenomena in Gases. New York: American Elsevier Publishing Co., 1965.
24. Price, W. J. Nucleonics Instrumentation (a preliminary manuscript for Chapters 1 through 5), unpublished text. School of Engineering, Air Force Institute of Technology, Wright-Patterson AFB, OH.
25. Shibamura, E., et al. "Drift Velocities of Electrons, Saturation Characteristics of Ionization and W-Values for Conversion Electrons in Liquid Argon, Liquid Argon-Gas Mixtures and Liquid Xenon," Nuclear Instruments and Methods, 131: 249-258 (1975).
26. Wilkinson, D. H. Ionization Chambers and Counters. New York: Cambridge University Press, 1950.

### Appendix: Discharge in Gases

Since the argon or xenon is in gaseous form between the anode and the grid, the breakdown potential of these gases limits the magnitude of the electric fields used in the chamber. Breakdown occurs when the following condition is met (23:115).

$$\gamma(\exp(\alpha d) - 1) = 1 \quad (26)$$

where

$d$  is the distance between the electrodes

$\alpha$  and  $\gamma$  are the Townsend coefficients

Alpha is a measure of the number of ion pairs produced in the gas given a certain electric field. Alpha can be found from Figure 20 with the equation

$$\eta = \alpha E/p \quad (27)$$

where

$\eta$  is the ionization coefficient in ion pairs per volt

$E$  is the electric field in V/cm

$p$  is the gas pressure in mm Hg

The secondary emission coefficient,  $\gamma$ , depends on the gas and the composition of the electrodes. Figure 21 gives values of  $\gamma$  for values of electric field divided by gas pressure. The bias voltages required to cause discharge are shown graphically by the Paschen curves in Figure 22.

In order to avoid discharges the vapor pressure of the liquid noble gas in the chamber must be above a certain point or below a certain point.

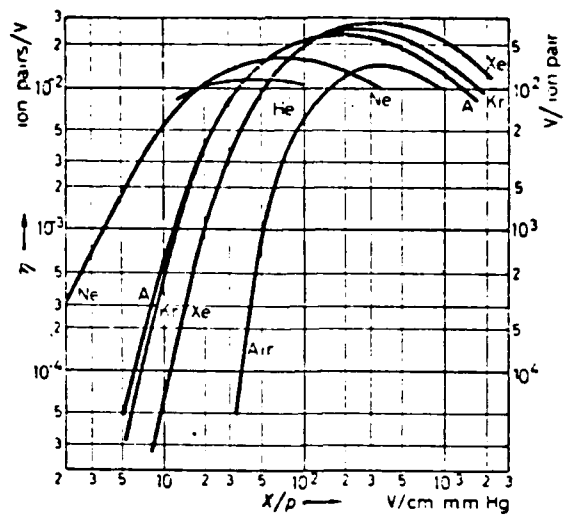


Fig. 20. The Ionization Coefficient in Various Gases (10:44)

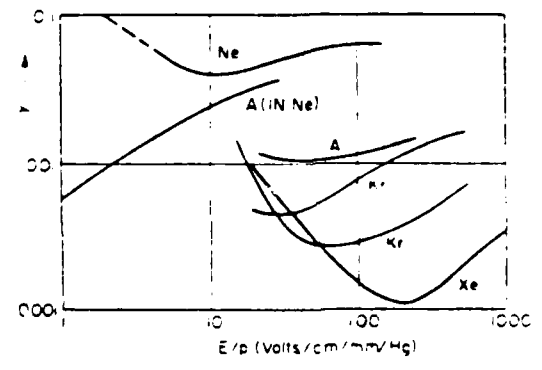


Fig. 21. The Secondary Emission Coefficient (7:4-17)

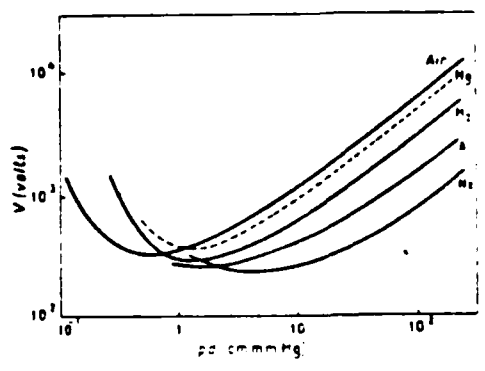


Fig. 22. Paschen Curves (1:3:11)

In the chamber under study the grid to anode distance is 0.55 cm. The chamber is usually operated with a liquid argon vapor pressure of 480 mm Hg. Figure 22 indicates a breakdown voltage of approximately 3000 V.

The approximate value of the breakdown voltage is used to determine a more accurate value. With this value of  $E/p$  near 11.4,  $\gamma$  can be determined from Figure 21 to be 0.07, and  $\eta$  is  $9 \times 10^{-4}$  ip/V. By manipulation of equation (26)  $\alpha$  is solved for as

$$\alpha = \ln(1 + 1/\gamma)/d \quad (28)$$

The value of  $\alpha$  in this case is 4.96 ip/cm. Using  $\eta$  the breakdown voltage is found as 5500 V/cm. Through further iterations the breakdown voltage is estimated as 3800 V/cm.

VITA

Matthew R. Gibbons was born in Detroit, Michigan on July 23, 1960. He graduated from high school in Woodstock, Illinois in 1978. He attended Purdue University from which he received a Bachelor of Science degree in Physics in May 1982. Upon graduation he was commissioned as an officer in the USAF through the ROTC program. He entered active duty in August 1982 and entered the School of Engineering, Air Force Institute of Technology.

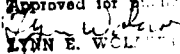
Permanent address: 1698 Woodside Court

Woodstock, Illinois 60098

UNCLASSIFIED

SECURITY CLASSIFICATION OF THIS PAGE

## REPORT DOCUMENTATION PAGE

1a. REPORT SECURITY CLASSIFICATION UNCLASSIFIED		1b. RESTRICTIVE MARKINGS	
2a. SECURITY CLASSIFICATION AUTHORITY		3. DISTRIBUTION/AVAILABILITY OF REPORT Approved for public release; distribution unlimited.	
2b. DECLASSIFICATION/DOWNGRADING SCHEDULE			
4. PERFORMING ORGANIZATION REPORT NUMBER(S) AFIT/GNE/PH/84M-3		5. MONITORING ORGANIZATION REPORT NUMBER(S)	
6a. NAME OF PERFORMING ORGANIZATION School of Engineering	6b. OFFICE SYMBOL (If applicable) AFIT/ENP	7a. NAME OF MONITORING ORGANIZATION	
6c. ADDRESS (City, State and ZIP Code) Air Force Institute of Technology Wright-Patterson AFB, Ohio 45433		7b. ADDRESS (City, State and ZIP Code)	
8a. NAME OF FUNDING/SPONSORING ORGANIZATION	8b. OFFICE SYMBOL (If applicable)	9. PROCUREMENT INSTRUMENT IDENTIFICATION NUMBER	
8c. ADDRESS (City, State and ZIP Code)		10. SOURCE OF FUNDING NOS.	
		PROGRAM ELEMENT NO.	PROJECT NO.
		TASK NO.	WORK UNIT NO.
11. TITLE (Include Security Classification) See Box 19			
12. PERSONAL AUTHOR(S) Matthew R. Gibbons, B.S., 2d Lt, USAF			
13a. TYPE OF REPORT MS Thesis	13b. TIME COVERED FROM _____ TO _____	14. DATE OF REPORT (Yr., Mo., Day) 1984 March	15. PAGE COUNT 67
16. SUPPLEMENTARY NOTATION			
17. COSATI CODES		18. SUBJECT TERMS (Continue on reverse if necessary and identify by block number)	
FIELD	GROUP	SUB. GR.	
18	04		
18	02		
19. ABSTRACT (Continue on reverse if necessary and identify by block number)			
Title: Evaluation of a Gridded Ionization Chamber for the Detection of Radioactive Noble Gases			
Thesis Chairman: Dr. George John			
<p>Approved for public release: LAW AFR 190-174            LYNN E. WOLCOTT, AF 681          Dean for Research and Professional Development          Air Force Institute of Technology (AFIT)          Wright-Patterson AFB, OH 45433</p>			
20. DISTRIBUTION/AVAILABILITY OF ABSTRACT UNCLASSIFIED/UNLIMITED <input checked="" type="checkbox"/> SAME AS RPT. <input type="checkbox"/> DTIC USERS <input type="checkbox"/>		21. ABSTRACT SECURITY CLASSIFICATION UNCLASSIFIED	
22a. NAME OF RESPONSIBLE INDIVIDUAL Dr. George John	22b. TELEPHONE NUMBER (Include Area Code) 513-255-5533	22c. OFFICE SYMBOL AFIT/ENP	

DD FORM 1473, 83 APR

EDITION OF 1 JAN 73 IS OBSOLETE.

UNCLASSIFIED  
SECURITY CLASSIFICATION OF THIS PAGE

This study investigates the feasibility of quantifying the constituents of a radioactive noble gas sample with a liquid noble gas gridded ionization chamber. Xenon-131m and xenon-133 are the noble gases used to test the chamber. Several other sources are used to characterize other aspects of the chamber. The chamber is designed to hold the liquid noble gas between the cathode and the grid while vapor remains between the anode and the grid. Thus the ionization caused by the radioactive noble gas sample is confined for the most part between the grid and the cathode. In this way position dependence of generated voltage pulse heights is eliminated. The efficiencies found for the detector are high, but the energy resolution is only 40% fwhm. The poor resolution is due to limited electric fields in the chamber, 2.4 kV/cm. Discharge in the vapor prevented higher electric fields in the chamber. Without good energy resolution, ratios of radioactive nobles in a sample can not be found. Some possible solutions to the energy resolution problem are presented.

**END**

**FILMED**

**4-85**

**DTIC**